Master's thesis

NTNU
Norwegian University of Science and Technology
Faculty of Engineering
Department of Marine Technology

Håkon Teigland

Dynamic Positioning of Surface Effect Ships using vent valve actuation

Master's thesis in Marine Technology
Supervisor: Vahid Hassani
June 2019

NTNU
Norwegian University of
Science and Technology

Håkon Teigland

Dynamic Positioning of Surface Effect Ships using vent valve actuation

Master's thesis in Marine Technology
Supervisor: Vahid Hassani
June 2019

Norwegian University of Science and Technology
Faculty of Engineering
Department of Marine Technology

NTNU
Kunnskap for en bedre verden

Preface

This thesis has been part of a project that is the result of a collaborative effort of SINTEF Ocean, Umoe Mandal, and NTNU-AMOS; the project was supported in part by the MAROFF program for research, innovation, and sustainability within marine and offshore industries (Project No. 282404). The Norwegian Research Council is acknowledged as the main sponsor of AMOS.

Specifically, the task of this thesis was to develop a DP controller and thrust allocation for Surface Effect Ships using vent valve actuation. In addition to this thesis, this task has resulted in two conference papers submitted for publication.

I would like to express my thanks to my main supervisor Vahid Hassani and co-supervisor Øyvind Auestad from Umoe Mandal for all help during the work on the thesis. I am also very grateful for the opportunity to take part in experimental testing, which has given me a lot of insight into the practical considerations when implementing a control system on a physical system.

Abstract

For an offshore worker in the oil and gas industry, the helicopter transport to the installation is the activity associated with the highest risk. An alternative to helicopter crew transfers is to use Surface Effect Ships (SES). A SES is a catamaran vessel carried in part by a pressurized air cushion. The pressure is maintained by fans and controlled using vent valves that control the airflow out of the cushion. During crew transfer from the SES to the offshore installation, the position of the SES needs to be maintained with a Dynamic Positioning (DP) system. By mounting the vent valves on the hull sides, the thrust force coming from the air exiting the vent valves can be used for actuation in the DP system. This would reduce the required installation power and operational cost of the DP system. Furthermore, combining the thrust from the vent valves with DP thrusters would give a DP system with a high degree of redundancy since thrust force may be generated from two different physical principles.

This thesis presents a sway-yaw control system for a SES that is actuated purely by vent valve thrust from the pressurized cushion. The control system is verified using simulations and experimental model-scale testing in an ocean basin. For such a vent valve DP system to work, it is important to have a thrust force model. Therefore, this thesis also investigates two thrust force models. Both models are compared to CFD analyses and experimental tests.

The control system and the principle of using thrust force from vent valves have been shown to work. Although implementation details would need to be addressed, the control system should work on a full-scale SES. The benefit of the control system is that it is very simple and requires no alternations when it has been tuned properly, which should be relatively simple since there are few gains and parameters to be tuned.

Both thrust models provide a practical estimate of the thrust force from a vent valve at maximum valve opening, but only one of the models seems to give an acceptable thrust force estimate for all vent valve openings.

Although more work on this subject would provide useful insight, especially with regards to the generated thrust force and the geometry and layout of the vent valve system, the proposed system could serve as a basis for implementation on a full-scale SES.

Nomenclature

α	Kinetic energy correction factor, fitting parameter, scaling factor
$\dot{\theta}$	Angular pitch rate
$\dot{\zeta}$	Wave profile rate
$\dot{z}$	Heave velocity
ϵ	Ratio between vent side length and total valve louver thickness
η	Vessel position in NED frame
η^p	Vessel position in parallel reference frame
η^p_r	Vessel reference position in parallel reference frame
γ	JONSWAP peakedness parameter, Ratio of specific heats for air
$\hat{T}$	Estimated wave period
ν	Body fixed translational and angular velocities
ω_0	Central cutoff frequency
ω_p	Peak frequency
ρ	Density of air
σ	JONSWAP width parameter
τ_c	Air cushion forces
τ_{env}	Environmental forces
Θ	Orientation in the NED frame
θ	Vent valve opening angle
a	Acceleration
A_∞	Added mass matrix at infinite frequency
A_L	Vent valve leakage area
A_v	Vent area
c_n	Orifice coefficient
$C_A(\nu)$	Added Coriolis-centripetal matrix
$C_{RB}(\nu)$	Rigid-body Coriolis-centripetal matrix
CG	Center of gravity
D	Nonlinear damping matrix

$D(\nu)$	Damping matrix
DOF	Degree of freedom
f	Thrust force
f_1	First thrust model
f_2	Second thrust model
G	Stiffness matrix
h	Head loss
h_f	Major head loss
h_m	Minor head loss
H_s	Significant wave height
$J(\Theta)$	Transformation matrix relating η and ν
K	Loss coefficient
K_c	Constant loss coefficient
K_v	Valve loss coefficient
L	Vent duct length
M	Rigid body mass matrix
m	Mass
m_i	i^{th} spectral moment
M_A	Added mass matrix
M_{RB}	Rigid-body mass matrix
n_l	Number of vent valve louvers
p	Excess cushion pressure
p	Position in the North-East-Down (NED) frame
p_0	Equilibrium excess cushion pressure
p_a	Atmospheric pressure
Q	Volumetric flow rate, notch width factor
S	Ocean wave spectrum
s	Vent side length
T_h	Higher wave period design limit

T_l	Lower wave period design limit
T_y	Measured zero up-crossing period
v	Velocity
V_c	Cushion volume
x_{cp}	Longitudinal distance between cushion pressure center and vessel CG

Contents

1 Introduction

1.1 Background and motivation

The Norwegian offshore oil and gas industry has a high focus on safety with the main actor, Equinor, aiming to be the industrial leaders in safety [1]. However, personnel transport is mainly done by helicopter, despite it being one of the most high-risk activities for an offshore worker [2]. An alternative to crew transfers by helicopter is to use Crew Transfer Vessels (CTVs). One type of CTV used for crew transfers of service personnel for offshore wind turbines is the Surface Effect Ship (SES).

A SES is a catamaran vessel carried in part by a pressurized air cushion and in part by two side hulls. The pressurized cushion is created by fans that blow air into the volume under the deck. The cushion is sealed off at the bow by so-called finger skirts and at the aft by the so-called aft lobe bag, as shown in Fig. 1. The propulsion is typically provided by a water jet with vector sleeves and reversible buckets. A detailed description of the SESs is given by Butler in [3].

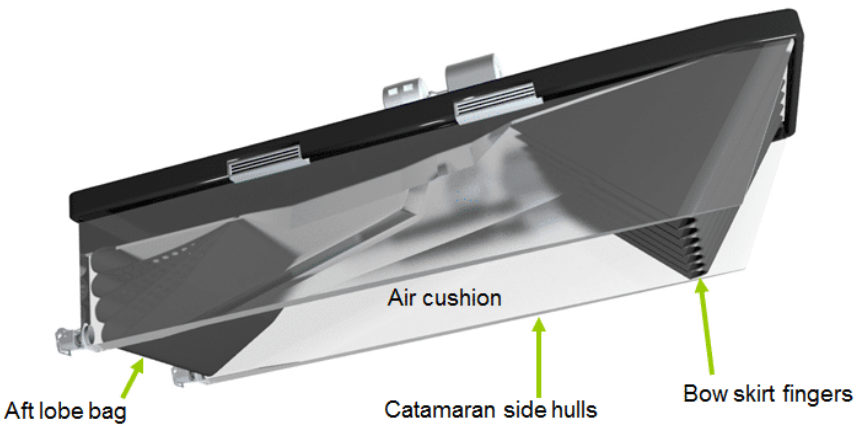

Figure 1: SES concept, by courtesy of Umoe Mandal.

The traditional main benefit of a SES is the high transit speed due to low hydrodynamic resistance. The low resistance is possible by pressurizing the air cushion which lifts the majority of the hull out of the water and enables a decreased draft. One of the drawbacks of a SES is it is subject to an undesired effect called the cobblestone effect. The cobblestone effect is a high-frequency oscillation in heave that occurs at certain encounter frequencies. By controlling the airflow out of the cushion, the pressure can be controlled to limit the cobblestone effect [4]. Such a system is known as a Ride Control System (RCS). The airflow out of the cushion is controlled by adjusting square butterfly type valves, or louvers, that are installed in ducts connecting the cushion to ambient pressure, such as the ones installed on the scale model in Fig. 2.

If these vessels are to be used as CTVs for the offshore oil and gas industry on the Norwegian Continental Shelf (NCS), it is required that the vessel can maintain a fixed position and heading during the transfer operation. One possible solution is to install a Dynamic Positioning (DP) system. Such a system typically uses thrusters and propellers to maintain the desired position and

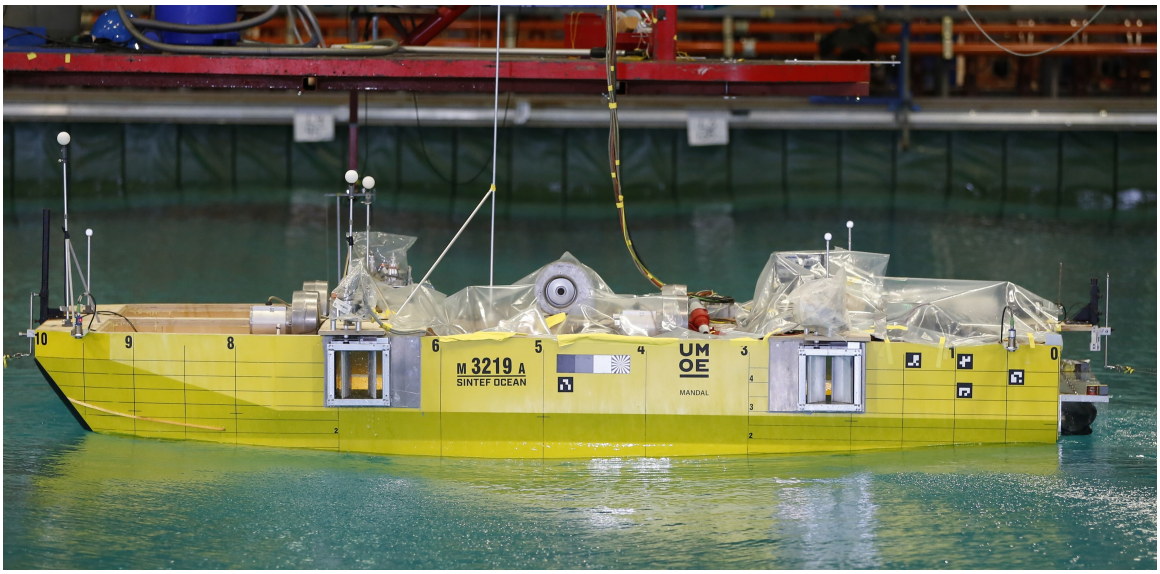

Figure 2: Scale model B in the ocean basin at SINTEF Ocean.

heading. However, by exploiting the pressure difference between the cushion and the atmosphere, vents installed on the hull sides may be used to provide thrust in sway and yaw.

Class societies divide DP systems into classes. DNV-GL divide DP systems into DPS1, DPS2 and DPS3 [5], the main difference being the level of redundancy. For oil and gas, the industry standard is DPS2 and DPS3, which both require redundancy in technical design. For the DP system on a SES, DPS1 could in principle be achieved using the vent valve thrust alone. However, any practical implementation would likely be a combination of vent valves and the prime mover. Because the vent valves need to be installed for the RCS, the cost of such a DP system would be low.

DPS2 or DPS3 on a SES would probably require additional thrusters to be installed. However, since these DP classes require redundancy, the cost of the DP system would likely be significantly less by using the vent valves as part of the DP systems. More importantly, the main causes of DP incidents from 2011 to 2016 have been attributed to thruster failures [6]. Thus, being able to provide thrust from a system that does not rely on rotating thrusters, but is based on a different physical principle provides true redundancy.

A final motivation for a vent valve DP system is the operational cost. To obtain desired motion characteristics at low speed, a SES is usually operated around a mean cushion pressure. In practice, this is done by running the fans at a constant speed and varying the mean valve positions (bias) such that each valve has the same opening. Thus, some of the thrust required for the DP system will come at no increase in fuel consumption.

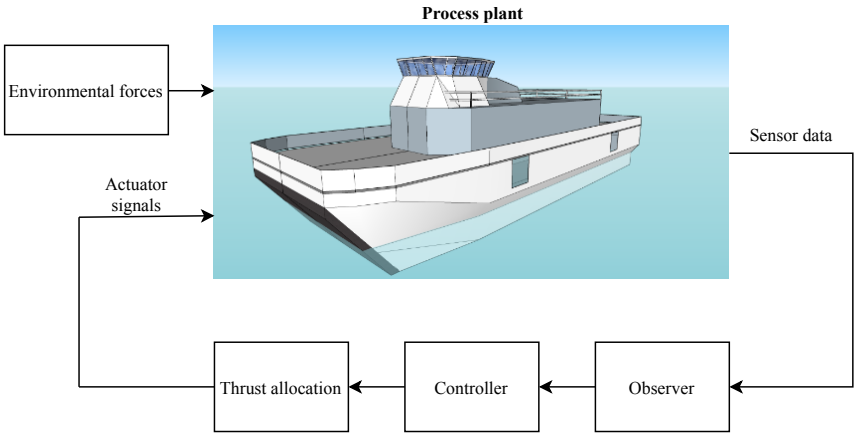

Figure 3: DP system overview.

1.2 Previous work

1.2.1 Dynamic Positioning

As the offshore oil industry started to drill for oil at larger depths, fixed structures became unfeasible and floating drilling units had to be used. However, fixing the position by mooring the unit to the seabed gave rise to other challenges. A solution was to keep the position by manually controlling propellers and thrusters. Since this was difficult and tedious, the first DP systems came into use in the 1960s [7]. Although these were very simple, the principle of a DP system is the same today. A modern DP system usually consists of at least an observer, controller, and thrust allocation, as the schematic in Fig. 3 shows.

The main purpose of the observer is to filter signal noise and usually also first-order wave frequency motion. This is to avoid having to install large actuators and to spare the installed actuators. Several observer algorithms exist, but they are typically based on notch filters or Kalman filters. Since the Kalman filter leads to a large number of tuning parameters Fossen and Strand [8] presents a nonlinear observer that can be tuned using relatively few gains.

The controller is responsible for determining the actuation force based on the filtered position, velocity and acceleration measurements. Typical control designs use a nonlinear PID that accounts for the heading of the vessel. Sørensen [9] propose an additional stiffness term that is proportional to the cubed position error. More advanced control designs use hybrid control. For example, [10] propose a hybrid control scheme of DP vessels to extend the weather window for offshore operations.

The primary objective of the thrust allocation is to command the desired force from the controller using the available actuators. The thrust allocation is usually designed such that it minimizes the actuation force or power consumption. The thrust allocation must also be able to account for physical actuator limitations like rotational speeds, thrust sectors, etc. To achieve this, [11] shows how optimization by Lagrange multipliers may be used to minimize the actuation force while satisfying the commanded forces from the controller. However, this approach is unable to account

for constraints. Other optimization techniques may be used, but these are often computationally expensive and not suited for implementation on real-time control systems. One solution that use quadratic programming and allows for much of the computation to be performed offline is presented in [12].

1.2.2 Ride Control System

RCSs are used to stop high-frequency oscillations in heave and pitch that occur during medium-to-high-speed transits. The RCS damps the encountered sea wave frequency and certain air cushion resonances. These resonances are due to a coupling between heave, pitch and pressure. The oscillations are reduced by manipulating the pressure in the cushion. Controlling the pressure can in principle be done by controlling the airflow into the cushion, but since this would put very high demands on the fans pressurizing the cushion, the practical solution is to control the airflow out of the cushion. [4] presents a RCS that is designed using dissipative control and is able to reduce vertical accelerations by accounting for spatial and non-spatial varying pressure resonances.

1.2.3 Boarding Control System

Inspired by the RCS, Auestad [13] presents a Boarding Control System (BCS) to eliminate bow motions of the SES, making boarding safer and more convenient. Today, this system is used on Umoe Mandal's CTVs for the transport of service personnel to offshore wind turbines. Surge motion is eliminated by using the main propulsion to push onto the windmill while heave and pitch motion are reduced by controlling the airflow out of the cushion. By careful placement of the motion sensors, the BCS will insure that the vessel rotates, in pitch, about the contact point between bow-fender and the wind turbine.

1.2.4 Vent valve lateral control

[14] investigates using vent valves for lateral control of a SES and proposes a systematic procedure for designing robust controllers to control the sway motion of a SES. The proposed controller design is based on H_∞ techniques, which were introduced for the robust design of control systems by Zames [15]. The purpose of these techniques is to design robust controllers in the sense that stabilization for some disturbance or plant uncertainty is guaranteed. When using H_∞ techniques, the control problem is formulated as a mathematical optimization problem.

Except for a Master Thesis exploring vent valves and water jets to perform stationkeeping [16], little work has been done on the subject of motion control using the thrust force from vent valves on SESs.

1.3 Contribution of the thesis

This thesis presents a sway-yaw control system for a SES that is actuated purely by vent valve thrust from the pressurized cushion. The control system is verified using simulations and experimental

model-scale testing in an ocean basin. For such a vent valve DP system to work, it is important to have a thrust force model. Therefore, this thesis also investigates two thrust force models. Both models are compared to CFD analyses and experimental tests.

2 Vent valve thrust force

2.1 Thrust model 1

To derive the first model for thrust force from the vent valves, consider a vent with a square cross-section and a valve consisting of adjustable louvers, as illustrated in Fig. 4. The inlet of the vent valve is connected to the pressurized air cushion in the SES, while the outlet is open to atmospheric pressure. The flow velocity is assumed to be zero at the inlet, v_c at the center of the valves and the flow exits the vent with velocity v_{out} and volumetric flow rate Q_{out}. The excess pressure, or pressure difference, between the cushion and atmosphere is p and it is assumed that there is atmospheric pressure at the center of the valve.

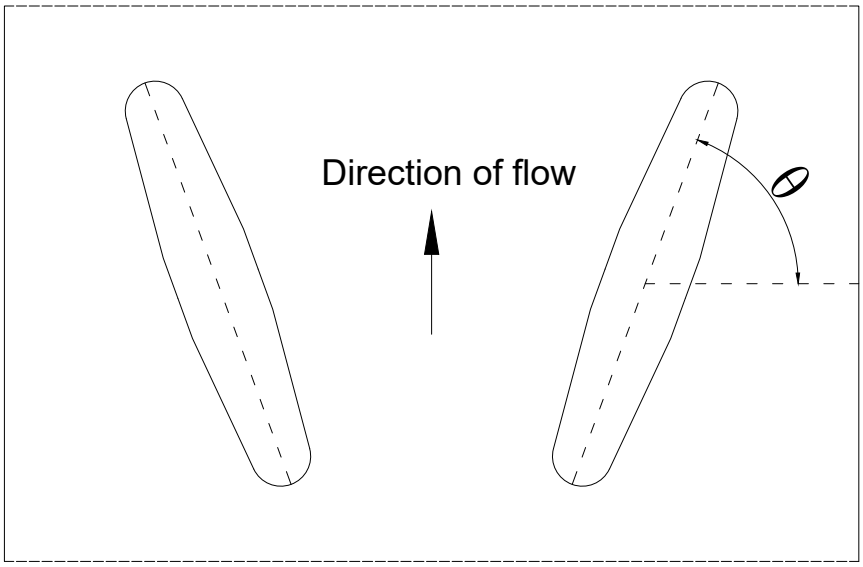

Figure 4: Top view of a vent valve.

From Newton's second law with the assumption of steady-state and in-compressible flow, the thrust force from a vent valve is

$$f = \frac{d}{dt}(mv) = \rho Q_{out} v_{out} \tag{1}$$

The first thrust model assumes that the valves in the vent are simplified to the projected area as seen along the direction of flow. Bernoulli's principle relates the cushion pressure to the velocity

at the center of the valves such that

$$\frac{p}{\rho} = \frac{v_c^2}{2} \tag{2}$$

To account for any losses, the orifice coefficient c_n is introduced such that the velocity at the center of the valves is

$$v_c = c_n \sqrt{\frac{2p}{\rho}} \tag{3}$$

From the velocity at the center of the valves, the volumetric flow rate at the center and consequently at the outlet due to continuity is

$$Q_{out} = c_n \sqrt{\frac{2p}{\rho}} A_L \tag{4}$$

where A_L is the vent valve leakage area.

From continuity and the assumption of incompressible flow

$$v_{out} A_v = Q_{out} \tag{5}$$

where A_v is the vent area, such that the velocity at the outlet in terms of the excess cushion pressure is

$$v_{out} = \frac{A_L}{A_v} c_n \sqrt{\frac{2p}{\rho}} \tag{6}$$

Finally, inserting (6) into Newton's second law, the first model for thrust force from a vent valve is obtained as

$$f_1 = 2c_n^2 p \frac{A_L^2}{A_v} \tag{7}$$

Since this model is based on flow through an orifice, the leakage area for a square vent valve with side length s and n_l louvers that are s/n_l wide and $\epsilon s/n_l$ thick, may be expressed in terms of the opening angle as

$$\begin{aligned} A_L &= A_v - \left(\frac{s}{n_l} \cos\theta + \frac{\epsilon s}{n_l} \sin\theta \right) s n_l \\ &= (1 - \cos\theta - \epsilon \sin\theta) s^2 \end{aligned} \tag{8}$$

Then,

$$f_1 = 2c_n^2 p s^2 (1 - \cos\theta - \epsilon \sin\theta)^2 \tag{9}$$

The first thrust model is derived based on flow through an orifice. As such, it is highly simplified. However, RCS designs typically use (4) to model the airflow out of the vent valves, see e.g. [17] and [4], and [13] presents a heave control system that use (4). Details on the mathematical modeling of the coupled vessel and pressure cushion dynamics that are used in the work mentioned are given by [18]. Although the analysis by Steen is very detailed, the airflow out of the cushion is based on (4) with an orifice coefficient assumed to vary between 0.61 and 1, based on results by [19].

2.1.1 Thrust model 2

An alternative approach to determine the velocity exiting a vent valve is to start from the steady flow equation as presented by [20],

$$\left(\frac{p}{\rho g} + \frac{\alpha v^2}{2g} + z\right)_{out} = \left(\frac{p}{\rho g} + \frac{\alpha v^2}{2g} + z\right)_{in} + h \tag{10}$$

where α is a kinetic energy correction factor which is approximately 1 for turbulent flow. h represents the losses in the system and may be written as the sum of the friction loss between the fluid and the duct h_f and other losses h_m,

$$h = h_f + \sum h_m = \frac{v^2}{2g}\left(f\frac{L}{s} + \sum K\right) \tag{11}$$

In the above equation, f is the Darcy friction factor which is a function of Reynold's number and pipe roughness. L/s is the length to width ratio of the duct and K is a loss coefficient determined from the loss across artifacts such as bends, edges, and valves by

$$K = \frac{v_{in}^2 - v_{out}^2}{2g} = \frac{p_{in} - p_{out}}{\rho g} \tag{12}$$

For the vent valve system on a SES, there are losses due to the valve, bends and the contraction from the cushion to the ducts. The loss due to the valve grows almost exponentially with closing angle and approach zero for full opening, depending on the width and shape of the valve ([20]). The loss due to the bends depends on the ratio between bend radius and duct width, such that increasing the radius reduces the loss coefficient. For a smooth pipe with a radius equal to the width, $K_{bend} \approx 0.25$. The loss due to a sudden contraction depends on the contraction ratio and approaches 0.42 as the ratio contraction ratio approaches zero. However, this is assuming sharp edges at the contraction. Thus, except for when the valves are fully open, the valves will dominate the minor losses. The loss for the relevant length to width ratios and frictions factors is very low, typically, $fL/s < 0.05$ and the static pressure loss is also negligible.

To derive a thrust model for varying vent valve angle, the loss coefficient is divided into a valve loss coefficient $K_v(\theta)$ and a constant loss coefficient K_c to account for the other losses in the system such that

$$K(\theta) = K_v(\theta) + K_c \tag{13}$$

Assuming that the flow exits the pipe with velocity v at atmospheric pressure and enters the pipe with zero velocity at pressure $p_{atm} + p$ and that all losses except the valve loss is neglected, (10) reduces to

$$\frac{p}{\rho g} = \frac{v^2}{2g} + \frac{v^2}{2g}K(\theta) \tag{14}$$

such that the outlet velocity is

$$v = \sqrt{\frac{2p}{\rho(1 + K(\theta))}} \tag{15}$$

Inserting into Newton's second law, the second model for thrust force from one vent valve is

$$f_2 = \frac{2p}{(1 + K(\theta))} A_v \tag{16}$$

3 SES Simulator

Verification of the sway-yaw control system has been performed by scale-model testing and through simulation. For simulation, a Simulink simulator called SESSim is used. SESSim has an overall configuration as shown in Fig. 5. The hydrodynamic coefficients of the vessel have been calculated using SINTEF's ShipX software and verification of the SESSim simulator has been done through experimental testing at SINTEF's towing tank. In the following section, the models used in the process plant and the environmental forces are explained.

3.1 Environmental forces

SESSim can simulate current, regular waves, and irregular waves that are generated from various spectra. When simulating waves, both first-order and second-order forces are calculated and sent to the process plant. From the generated waves, SESSim calculates the first order forces and the second order drift forces by using results obtained from ShipX.

The irregular sea states can be generated from the JONSWAP, ITTC or Torsethaugen ocean wave spectra. The JONSWAP spectrum was fitted to wave measurements from the North Sea by Hasselmann [21]. Starting from the Pierson-Moskowitz spectrum

$$S_{PM}(\omega) = \frac{\alpha g^2}{\omega^5} \exp\left(-\frac{5}{4}\left(\frac{\omega_p}{\omega}\right)^4\right) \tag{17}$$

where α is a scaling factor, then the JONSWAP spectrum is defined from S_{PM} by a peakedness parameter γ, such that

$$S_J = S_{PM}\gamma^{\exp\left(-\frac{1}{2}\left(\frac{(\omega-\omega_p)}{\sigma\omega_p}\right)^2\right)} \tag{18}$$

where

$$\sigma = \begin{cases} \sigma_a, & \text{for} \quad \omega \leq \omega_p \\ \sigma_b, & \text{for} \quad \omega > \omega_p \end{cases} \tag{19}$$

and σ_a and σ_b represents the width of the left and right sides of the spectrum, respectively. Hasselmann gives the following mean values for the spectral parameters

$$\gamma = 3.3, \quad \sigma_a = 0.07 \quad , \sigma_b = 0.09 \tag{20}$$

The mean value for γ should be used with care, as the distribution provided by Hasselmann shows that γ varies between 1 and 6.

The implementation of irregular waves in SESSim is done according to DNV-RP-C205 [22], which define the PM-spectrum as

$$S_{PM,DNV}(\omega) = m_0 \frac{S_{PM}}{\int_0^\infty S_{\mathrm{PM}}} = \frac{5\omega_p^4 H_s^2}{16\omega^5} \exp\left(-\frac{5}{4}\left(\frac{\omega_p}{\omega}\right)^4\right) \tag{21}$$

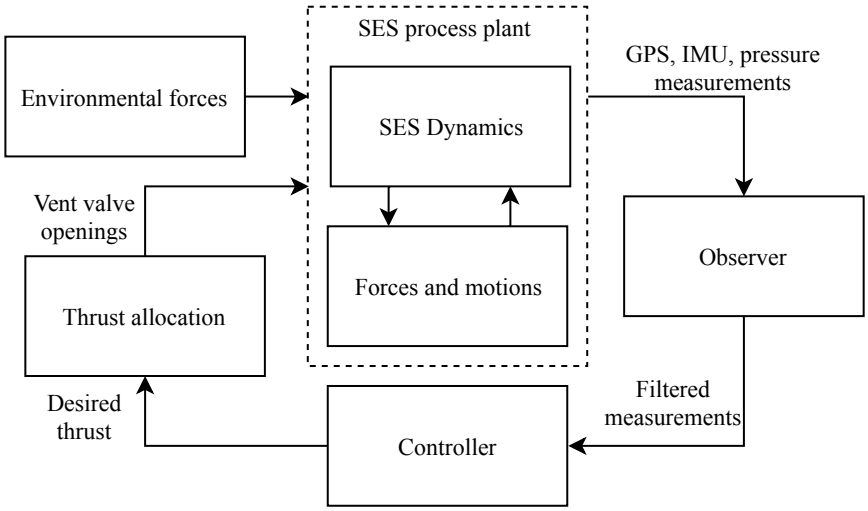

Figure 5: Overview of SESSim.

where m_0 is the zeroth moment of the spectrum and is related to the significant wave height H_s through

$$m_0^2 = \frac{H_s}{4} \tag{22}$$

when it is assumed that the wave heights are Rayleigh distributed. From the PM-spectrum, DNV define the JONSWAP spectrum as

$$S_{J,DNV} = (1 - 0.287 \ln \gamma) S_{PM,DNV}(\omega) \gamma^{\exp\left(-\frac{1}{2}\left(\frac{(\omega-\omega_p)}{\sigma\omega_p}\right)^2\right)} \tag{23}$$

When performing numerical realizations of ocean wave spectra it is common to set a lower and upper cutoff frequency to reduce the number of computations. Let ω_1 and ω_2 be the lower and upper cutoff frequencies, respectively. The zeroth moment of the PM-spectrum as calculated by DNV becomes

$$\begin{aligned} m_{0,PM,DNV}(\omega) &= \int_{\omega_1}^{\omega_2} \frac{5\omega_p^4 H_s^2}{16\omega^5} \exp\left(-\frac{5}{4}\left(\frac{\omega_p}{\omega}\right)^4\right) d\omega \\ &= \frac{H_s^2}{16}\left[\exp\left(-\frac{5}{4}\left(\frac{\omega_p}{\omega_2}\right)^4\right) - \exp\left(-\frac{5}{4}\left(\frac{\omega_p}{\omega_1}\right)^4\right)\right] \end{aligned} \tag{24}$$

Consequently, when generating irregular waves in SESSim one should be aware that the waves are smaller than what is expected from desired significant wave height. To fix this issue one could simply scale the spectrum to preserve the relation between the spectrum's zeroth moment and the significant wave height (22). When realizing the irregular sea states one should also take care to have sufficient amounts of frequencies, relative to the realization time, otherwise the wave profile will repeat itself.

3.1.1 Forces and motions

The six DOF vessel model is implemented as

$$\dot{\eta} = \begin{pmatrix} \dot{p} \\ \dot{\Theta} \end{pmatrix} = J(\Theta)\nu \tag{25a}$$

$$(M + A_\infty)\,\dot{\nu} + \left.\frac{\partial D}{\partial \nu}\right|_0 \nu + D\nu|\nu| + \mu + G\eta = \tau_{env} + \tau_c \tag{25b}$$

$$\dot{x} = A_r x + B_r \delta\nu \tag{25c}$$

$$\mu = C_r x + D_r \delta\nu \tag{25d}$$

where

p = Position in the North-East-Down (NED) frame

Θ = Orientation in the NED frame

ν = Body fixed translational and angular velocities

$J(\Theta)$ = Transformation matrix relating η and ν

M = Rigid body mass matrix

A_∞ = Added mass matrix at infinite frequency

D = Nonlinear damping matrix

G = Stiffness matrix

τ_{env} = Environmental forces

τ_c = Air cushion forces

μ in (25) accounts for the potential damping i.e. the fluid memory effects.

3.2 SES Dynamics

For an RCS, it is common to use linearized pressure models when modeling the cushion dynamics. However, an RCS typically operate close to an equilibrium pressure where linearization is an acceptable assumption. This is not the case for the sway-yaw control since the pressure may vary a lot due to the first order wave-body interaction. Therefore, the following nonlinear cushion dynamics is used in SESSim.

$$\dot{p} = \frac{\gamma\,(p_a + p)}{V_c}\left(\left(\frac{p_a + p_0}{p_a + p}\right)^{\frac{1}{\gamma}}(Q_{in} - Q_{out}) - \dot{V}_c\right) \tag{26}$$

where

p = Excess cushion pressure

p_a = Atmospheric pressure

p_0 = Equilibrium excess cushion pressure

γ = Ratio of specific heats for air

V_c = Air cushion volume

Q_{in} = Air flow into air cushion

Q_{out} = Air flow out from air cushion

In (26), the air flow from n_f fans, $Q_{in} = n_f q_{in}$, is nonlinear and taken from actual fan characteristics. The characteristics of a typical fan designed to operate under the maximum pressure p_{max} and maximum air flow Q_{max} may be modelled according to (Fig. 6)

$$q_{in} = q_{max} \left(\frac{p_{max} - p}{p_{max}} \right)^{1/2} \left(\frac{\omega_0}{\omega} \right)^2 \tag{27}$$

where ω_0 is the designed operation speed of the fan. Naturally, a real fan will deviate from (27), but the fan characteristics may be approximated by fitting

$$\widehat{q}_{in} = a q_{max} \left(\frac{p_{max} - p}{p_{max}} \right)^{1/b} \left(\frac{\omega_0}{\omega} \right)^2 \tag{28}$$

to the actual measurements, where a and b are parameters to be adjusted.

The air flow out Q_{out} results from the passive leakage area and active leakage area. The active leakage is due to the commanded valve positions and the passive leakage is all other leakage. with A_L being the total leakage area, the air flow out is

$$Q_{out} = c_n A_L \sqrt{\frac{2p}{\rho}} \tag{29}$$

The cushion dynamics is coupled to the heave and pitch motion of the SES through the changing cushion volume

$$\dot{V}_c = A_c \left(x_{cp} \dot{\theta} - \dot{z} - \dot{\zeta} \right) \tag{30}$$

where

x_{cp} = Longitudinal distance between cushion pressure center and vessel CG

$\dot{\theta}$ = Angular pitch rate

$\dot{z}$ = Heave velocity

$\dot{\zeta}$ = Wave profile rate

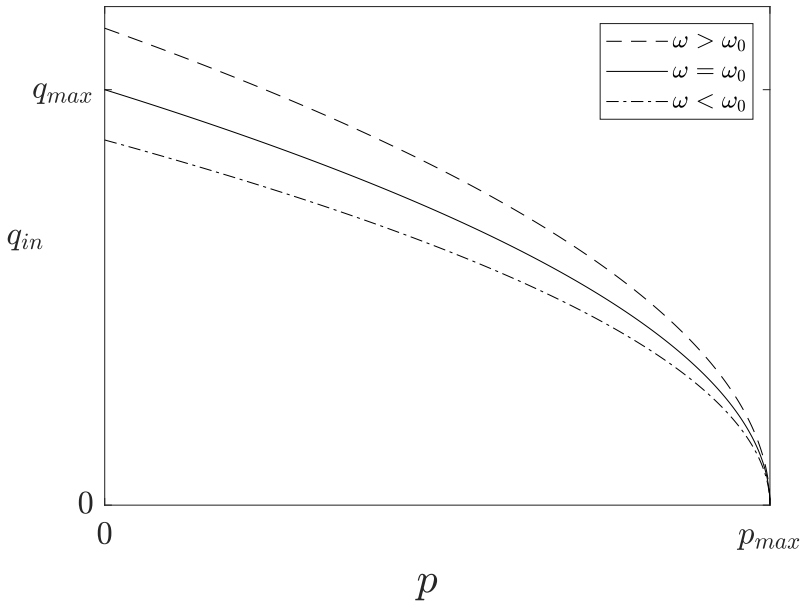

Figure 6: Typical fan characteristic curve.

4 Control System

For the purpose of control, the equations of motion is reduced to a sway-yaw two DOF system. To this end, let η^p contain the sway and yaw coordinates of the vessel in a reference parallel frame (Fig. 7), such that

$$\eta^p = \begin{pmatrix} -\sin\psi_r & \cos\psi_r & 0 \\ 0 & 0 & 1 \end{pmatrix} \begin{pmatrix} x \\ y \\ \psi \end{pmatrix} \tag{31}$$

where (x, y, ψ) is the position and heading of the vessel in the NED frame.

The control plant model is a linearized 2 DOF DP model ([23])

$$M\dot{\nu} = -D\nu + \tau + \tau_{env} \tag{32}$$

$$\dot{\eta}^p = \nu \tag{33}$$

where $M = M^\top > 0$ is the sway-yaw rigid body mass and added mass matrix and $D = D^\top > 0$ is the sway-yaw linearized damping matrix.

4.1 Observer

The sway-yaw controller aims to stop the vessel from moving in sway and yaw, when it is excited by environmental forces such as waves, wind and current. The position and orientation of the vessel

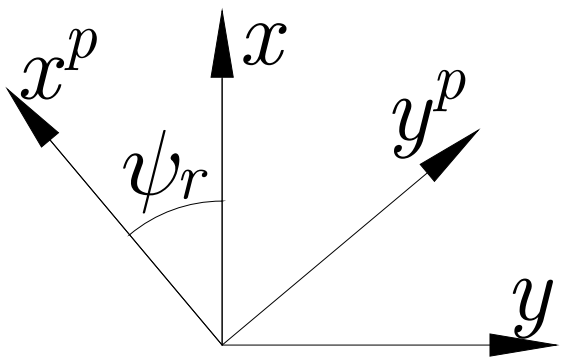

Figure 7: Frames used for the control plant model.

is measured by GPS while the translational acceleration and the angular velocities of the vessel is measured by an IMU. The wave forces are typically divided into first order forces and higher order forces. To limit the first order motions of the vessel one typically requires large amounts of thrust force. Therefore, the focus here is to compensate for the slowly-varying forces and mean force. To this end a notch filter is used to eliminate motions around the dominating wave frequency. An ordinary notch filter may be formulated as

$$H(s) = \frac{s^2 + \omega_0^2}{s^2 + \frac{\omega_0}{Q} s + \omega_0^2} \tag{34}$$

where ω_0 is the frequency to be rejected and the Q-factor determines how narrow the notch is, such that increasing the Q-factor leads to a narrower notch. The bode plot of (34) is shown in Fig. 8.

To determine ω_0, a frequency estimator is used. The frequency estimator works by measuring the time between zero up-crossings of the high-passed sway velocity and the sway velocity is obtained by integration of the sway acceleration. The estimated frequency $\hat{\omega}_0$ that is sent to the notch filter is the mean of the n_z most recent zero up-crossing measurements.

$$\frac{2\pi}{\hat{\omega}_0} = \widehat{T} = \frac{T_y(k - n_z - 1) + \cdots + T_y(k-1) + T_y(k)}{n_z} \tag{35}$$

In calm seas, it is not necessary to use the notch filter, so it is switched off if the variance of v_{hp} drops below a certain level.

The vessel is assumed to be operating in sea states within a range of wave periods $T \in [T_l, T_h]$. The Q-factor is tuned to T_l and T_h to determine a corresponding Q_l and Q_h, respectively. Note that the subscripts of Q_l and Q_h refers to the low and high limit of the wave period and therefore Q_l may be higher than Q_h. A linear relation between the Q-factor and the wave period is used such that the Q-factor for an arbitrary estimated wave period $\widehat{T}$ is

$$Q = \frac{\widehat{T} - T_l}{T_h - T_l} (Q_h - Q_l) + Q_l \tag{36}$$

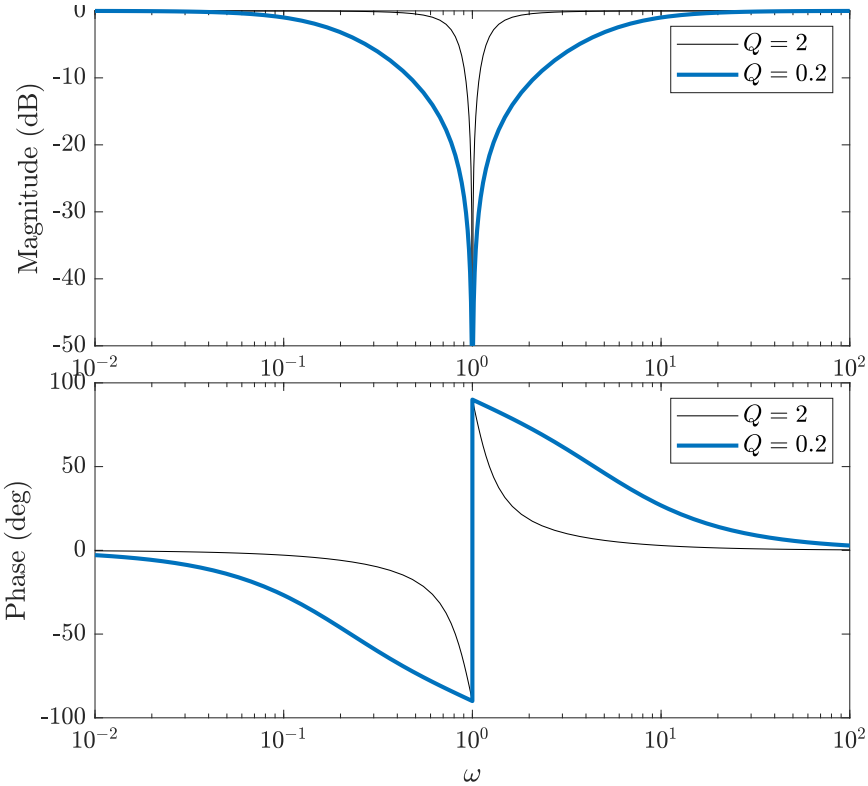

Figure 8: Bode plot of a notch filter for two different Q-factors.

4.2 Controller

A PID controller is used to control the sway and yaw motion of the SES and the control law is written as

$$\tau = -K_p\tilde{\eta}^p - K_d\nu - K_i z \tag{37}$$

where

$$\tilde{\eta}^p = \eta^p - \eta_r^p \quad \text{and} \quad z = \int \tilde{\eta}^p dt$$

and η_r^p is a constant desired reference for η^p.

To avoid integral windup, $\|z\|_\infty$ is non-increasing if any of the vent valves are fully open. The closed loop error dynamics of the unperturbed system become

$$\begin{aligned} M\dot{\nu} &= -\left(D + K_d\right)\nu - K_p\tilde{\eta}^p - K_i z \\ \dot{\tilde{\eta}}^p &= \nu \\ \dot{z} &= \tilde{\eta}^p \end{aligned} \tag{38}$$

Stability of (38) is shown by considering z as input to the system. The origin of the unforced system ($z = 0$) is shown to be stable by considering the positive definite Lyapunov function

$$V = \frac{1}{2}\left(\nu^\top M\nu + \tilde{\eta}^{p^\top} K_p\tilde{\eta}^p\right) \tag{39}$$

Taking the rate of V along the solution

$$\begin{aligned} \dot{V} &= -\nu^\top\left(D + K_d\right)\nu - \nu^\top K_p\tilde{\eta}^p + \tilde{\eta}^{p^\top} K_p\nu \\ &= -\nu^\top\left(D + K_d\right)\nu \leq 0 \end{aligned} \tag{40}$$

for $K_p = K_p^\top > 0$ and $K_d = K_d^\top > 0$. $\dot{V}$ is negative semi-definite and the only solution that can stay in the set $\{(\nu, \tilde{\eta}^p) \in \mathbb{R}^4 | \dot{V} = 0\}$ is the trivial solution $(\nu(t), \tilde{\eta}^p(t)) = 0$. Thus, according to the Krasovskii-LaSalle theorem, the unforced system is globally asymptotically stable (GAS). For linear systems, GAS implies global exponential stability (GES) and, as proved by [24], an unforced system that is globally Lipschitz and GES at the origin is input-to-state stable. Thus, (38) is input-to-state stable with z as input and z is bounded due to the anti-windup mechanism.

4.3 Thrust Allocation

4.3.1 General case

The force in 6 DOF from a vent k with thrust force f_k is

$$F_{surge} = -f_k \cos\alpha_k \cos\beta_k \tag{41}$$
$$F_{sway} = -f_k \sin\alpha_k \cos\beta_k \tag{42}$$
$$F_{heave} = f_k \sin\beta_k \tag{43}$$
$$M_{roll} = y^b_{v,k} F_{heave} - z^b_{v,k} F_{sway} \tag{44}$$
$$M_{pitch} = z^b_{v,k} F_{surge} - x^b_{v,k} F_{heave} \tag{45}$$
$$M_{yaw} = x^b_{v,k} F_{sway} - y^b_{v,k} F_{surge} \tag{46}$$

the resulting 2 DOF sway-yaw thrust vector is

$$\tau = \begin{pmatrix} F_{sway} \\ x^b_{v,k} F_{sway} - y^b_{v,k} F_{surge} \end{pmatrix} = -f_k \begin{pmatrix} \sin\alpha_k \cos\beta_k \\ x^b_{v,k} \sin\alpha_k \cos\beta_k - y^b_{v,k} \cos\alpha_k \cos\beta_k \end{pmatrix} \tag{47}$$

where α_k is the rotation of the vent about the z-axis and β_k is the rotation of the vent (Fig. 9) about the y-axis of a right-hand coordinate system with x-axis pointing to the bow and y-axis pointing to the starboard side. $x^b_{v,k}$ is the longitudinal coordinate of vent k, measured from a body-fixed coordinate system at the center of gravity.

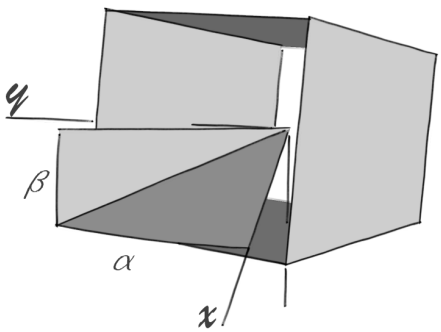

Figure 9: Vent angles.

For n multiple vents,

$$\tau = Tf = TKu = T_K u \tag{48}$$

where

$$K = diag\begin{pmatrix} K_1 & K_2 & \cdots & K_n \end{pmatrix} \quad \text{and} \quad u = A_L^{\circ 2}$$

and T is the thrust configuration matrix,

$$T = \begin{pmatrix} \sin\alpha_1 \cos\beta_1 & \cdots & \sin\alpha_n \cos\beta_n \\ x_{v,1}^b \sin\alpha_1 \cos\beta_1 - y_{v,1}^b \cos\alpha_1 \cos\beta_1 & \cdots & x_{v,n}^b \sin\alpha_n \cos\beta_n - y_{v,n}^b \cos\alpha_n \cos\beta_n \end{pmatrix}$$

To solve (48) for the input u one needs to find the inverse of T, but T is non-square. Fossen [23] use Lagrange multipliers to find a solution that satisfies (48) while minimizes the force f. Here it is desired to minimize the vent area A_L since the pressure drop is proportional to A_L. This is a nonlinear minimization problem and as a simplification, the minimization of u is performed. Thus, the minimization problem may be formulated as

$$J = \min_u \left(u^\top u\right) \qquad \text{s.t. } \tau - T_K u \tag{49}$$

The explicit solution may be found by defining the Lagrangian

$$L(u, \lambda) = u^\top u + \lambda^\top (\tau - T_K u) = u^\top u + \left(\tau^\top - u^\top T_K^\top\right) \lambda \tag{50}$$

with the derivative along the input u

$$\frac{\partial L}{\partial u} = 2u - T_K^\top \lambda = 0 \tag{51}$$

Inserting u from (51) into (48) gives

$$\tau = \frac{1}{2} T_K T_K^\top \lambda \tag{52}$$

which can be inserted into (51) with the assumption that the inverse of $T_K T_K^\top$ exists. Thus, the explicit solution to (48) that minimizes the squared leakage area is

$$u = T_K^\top \left(T_K T_K^\top\right)^{-1} \tau = T_K^\dagger \tau \tag{53}$$

where $T_K^\dagger$ is the Moore-Penrose pseudo-inverse of T_K.

Solving the thrust allocation problem by (53) may require unbounded inputs. Therefore, τ should in general be bounded before solving (53). An alternative approach is to use nonlinear programming or other numerical optimization.

In the case that the vent valves are combined with thrusters to obtain DPS2 or DPS3, the thrust allocation may be formulated as

$$\tau = TWf \tag{54}$$

where W is a weight matrix that is used to weight the various thrusters and vent valves and may be dependent on cushion pressure. As an example, consider a DP system on a SES with one vent valve on the port side and one vent valve on the starboard side, and additional thrusters. The sway is controlled in part by the vent valves and in part by the thrusters. The operator wants to stay at a bias of 50%, i.e. both valves should have a 50% opening. The thrust allocation algorithm might be designed such that the vent valves are used as long as the total airflow out corresponds to the 50% bias, while additional thrust is provided by the thrusters. This way, the fuel used to run the fans is used not only to maintain the correct cushion pressure but also to provide thrust.

4.3.2 Case study

The SES used in the case study has a vent configuration according to Fig. 10. The valves are equal and there is one pressure cushion. With this vent configuration, the thrust configuration matrix reduces to

$$T = \begin{pmatrix} 1 & -1 & 1 & -1 \\ l_{x,1} & -l_{x,1} & -l_{x,3} & l_{x,3} \end{pmatrix}$$

noting that $l_{x,1} = l_{x,2}$ and $l_{x,3} = l_{x,4}$. And the gain matrix may be replaced by a scalar gain

$$K = \frac{2c_n^2 p}{A_v} \tag{55}$$

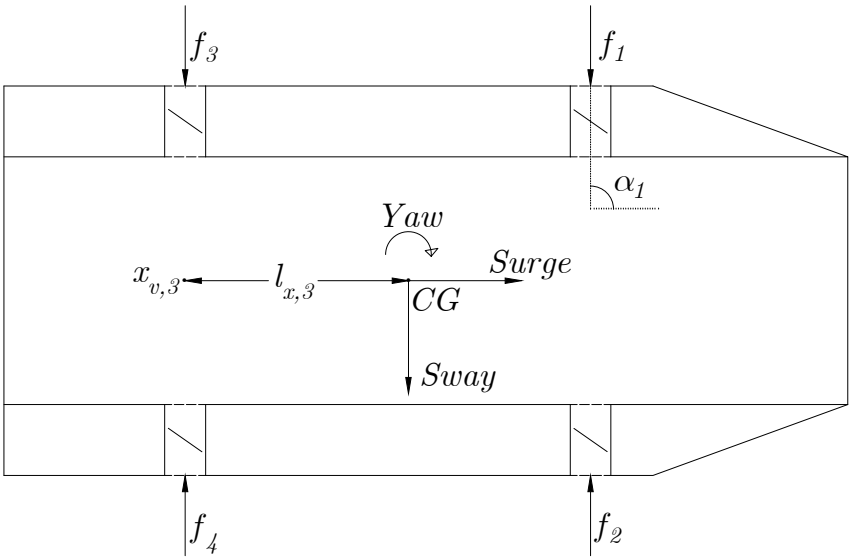

Figure 10: Top view of SES with vent configuration as in the studied case.

As mentioned previously, the pressure drop in the cushion is proportional to the leakage area. This means that to achieve maximum pressure, the optimal solution is found when only two valves are opened at a time. To determine which valves should be open, (53) is solved for τ. This will result in two valves with a positive opening and two valves with negative openings. Since there is no difference between positive and negative opening this determines which valves are open and which are closed. Let P be a binary matrix defined according to

$$P = \operatorname{diag}(u > 0) \tag{56}$$

Next, P is included into T_K by

$$\tilde{T}_K = T_K P \tag{57}$$

and the input is solved by

$$u = \tilde{T}_K^{\dagger} \tau \tag{58}$$

4.3.3 Implementation details

In the simulator and the experimental test setup, the valves are controlled by adjusting the angle of the valves from 0 to 100% ($0 - 90°$). The commanded angle for vent k is

$$u_{angle} = \arccos\left(1 - \frac{\sqrt{|u_k|}}{A_{v,k}}\right) \tag{59}$$

and the command sent to the actuators is

$$u_{cmd} = \frac{200}{\pi}\text{sgn}(u_k)u_{angle} \tag{60}$$

To avoid chattering at low vent valve angles, the commended valve positions are multiplied by a retardation function

$$r(u_{cmd}) = \exp\left(-\frac{100 + u_{cmd,bias}}{u_{cmd}^2}\right) \tag{61}$$

such that the chattering compensated input to the actuator is

$$u_{cmd}^* = r(u_{cmd})u_{cmd} \tag{62}$$

The effects of the implemented chattering compensation is provided in the results section.

5 Verification

5.1 Model testing

Two scale models have been used to verify the vent valve thrust force. The vents used on model A and B are shown in Figs. 11 and 2, respectively. Both of the vessels are model-scaled versions Umoe Mandal's SES designs. Vent valves, fans, finger skirt, and lobe bag are carefully scaled to represent the full-scale design. The experimental testing has been performed at SINTEF Ocean's laboratories.

The difference between the two models is mainly the vent valves and how the tests were performed. Model A has one vent valve on each side and the valves in the vents are three thin plates. Model B has two vent valves on each side and the valves in the vents are thicker but more rounded. Also, the vent valves model B has a better seal when the valves are closed and the testing of model A was performed with the model attached to a fixed arm, through a load cell, while the second model was floating freely, but connected to soft springs through load cells.

From the measured pressure p and force F obtained from the testing, the orifice coefficient and loss coefficient have been calculated as

$$c_n = \sqrt{F\frac{A_v}{2pA_L^2}} \tag{63}$$

and

$$K = \frac{2p}{F}A_v - 1 \tag{64}$$

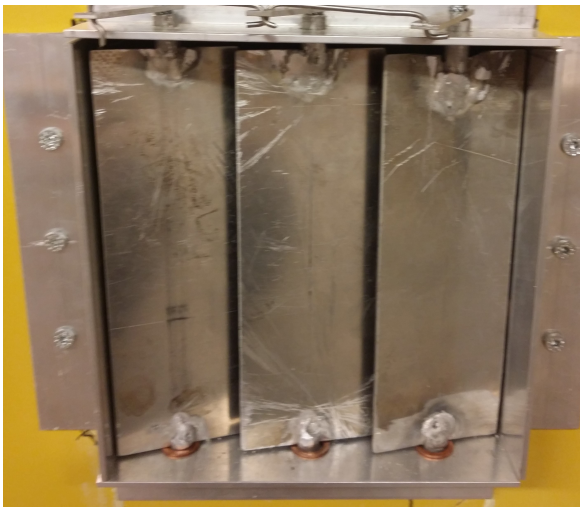

Figure 11: Vent valves on scale model A.

respectively.

Scale model B was fitted with a rigid wall along the centerline which divided the pressure cushion at large drafts. Since dividing the cushion along the center induces a roll angle and less pressure is provided for sway force, the thrust force test was performed at relatively high pressures. The high pressure lead to significant air leakage under the starboard hull at low valve angles. Also, during the tests on scale-model B, the valves were only allowed to go to a maximum opening angle of approximately 75°. Consequently, most of the results presented are from scale model A and the CFD analysis.

Testing of the sway-yaw control system was only performed on scale-model B.

5.2 CFD Analysis

CFD analysis of a vent valve system with valves modeled according to scale model B has been performed in Autodesk CFD. Analyses for various vent valve openings have been performed with fixed pressure as boundary conditions on the aft and forward cushion sides and zero pressure on the outlet. The pressure used for each vent valve opening has been determined by assuming frictionless flow out of the cushion. All analyses have been performed assuming steady state and incompressible flow.

From the outlet pressure p and velocity v obtained from the CFD analyses, the the orifice coefficient and loss coefficient have been calculated as

$$c_n = v\sqrt{\frac{\rho}{2p}}\frac{A_v}{A_L} \tag{65}$$

and

$$K = \frac{2p}{\rho v^2} - 1 \tag{66}$$

respectively.

6 Results

The results presented have been normalized due to commercial consideration. However, as the purpose of the thesis is to validate a concept, what is important is to show that the system works, not to give absolute performance results.

6.1 Simulation

6.1.1 Observer

The outputs from the notch filter and the frequency estimator when the SES is exposed to beam sea regular waves with a period of 8s (Fig. 12) and beam sea irregular waves following a JONSWAP spectrum with a peak period of 6s and peakedness factor 3.3 (Fig. 13).

For the case with beam sea regular waves with period 8s (Fig. 12), the waves are started at $t = t_1$. At $t = t_2$, the variance of v_{hp} exceeds the variance limit and the observer switches from using GPS measurements to using the notch filter. The frequency estimator converges quickly close to the wave period. The reason that the estimator is not constant after the first estimate is due to the transient that occurs when the waves first hit the SES. When the motion of the SES goes into steady-state, the frequency estimator starts to converge very close to the wave period. The notch filter is able to filter most of the first order sway motion. At $t = t_3$, the waves are turned off and at $t = t_4$, the variance of v_{hp} goes below the variance limit and the observer returns to using the GPS measurements. The same is seen for regular waves at other frequencies. The difference is that for longer waves, the frequency estimator uses more time to converge to the wave period. This is simply because fewer waves will be generated in the same amount of time as in the case with shorter wave periods, which leads to longer convergence times.

Fig. 13 shows the SES exposed to beam sea irregular waves generated from a JONSWAP spectrum with a peak period of 6s and peakedness factor of 3.3. The frequency estimator estimates periods between 5.2s and 6.9s. However, the estimate is below 6s for most of the simulation. The notch filter is able to filter much of the first order motions, but the filtering is worse for irregular waves than for regular waves. This is not surprising since the irregular sea state contains waves with frequencies around the peak frequency.

6.1.2 Step response

With no environmental forces acting on the SES, the response in sway and the desired and actual sway force for a step response are shown in Fig. 14. The sway position goes to the reference position

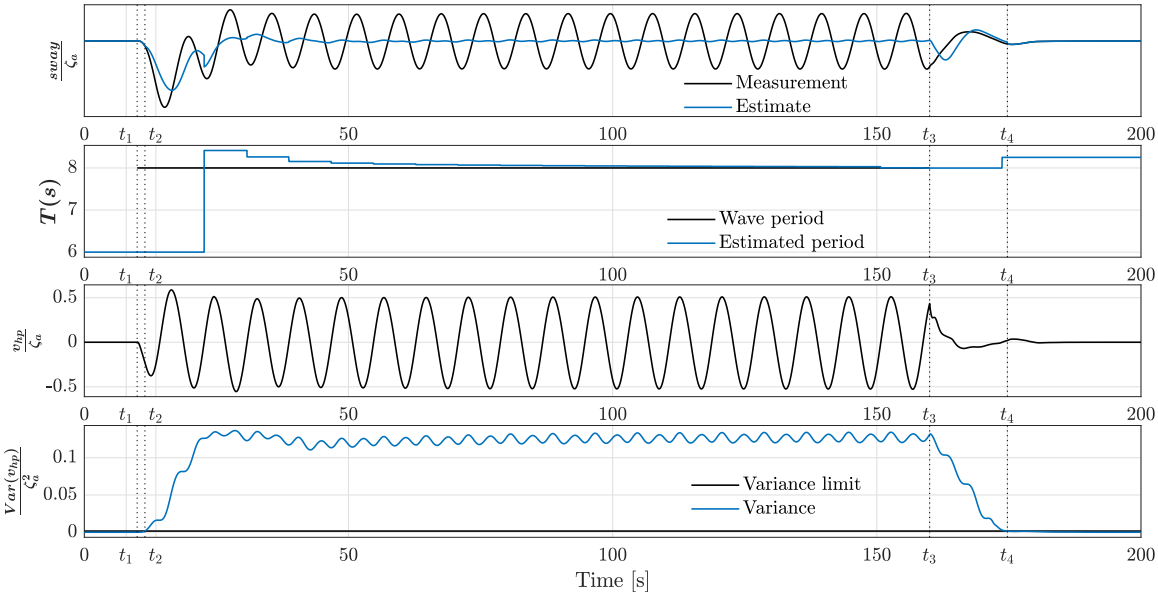

Figure 12: Observer and frequency estimator signals for beam 8s regular waves.

with an approximate overshoot of 10% of the initial offset. Most of the desired sway force is due to the proportional part of the PID control. The integral term gets saturated immediately. This is because the output sway force is below the desired sway force. At $t = t_1$, the desired sway force is equal to the output sway force and the integral term starts to change.

The vent valve openings during the sway step response are shown in Fig. 16. At the start of the simulation, the port vent valves are open to provide a sway force to the starboard side. The port forward vent valve is not fully open to provide the correct moment since the forward vents are placed further from the CG than the aft vents. At $t = t_1$, the port vent valve openings start to decrease and at $t = t_2$, the starboard vent valves are opened. This is because of the response overshoot seen in Fig. 14, which leads the controller to command a negative sway force.

The response in yaw for a 10° reference offset is shown in 15. The yaw response is practically the same as the sway response in Fig. 14. To control the SES to the desired heading, the port forward and the starboard aft vent valves are opened (Fig. 17) to provide a positive yaw moment.

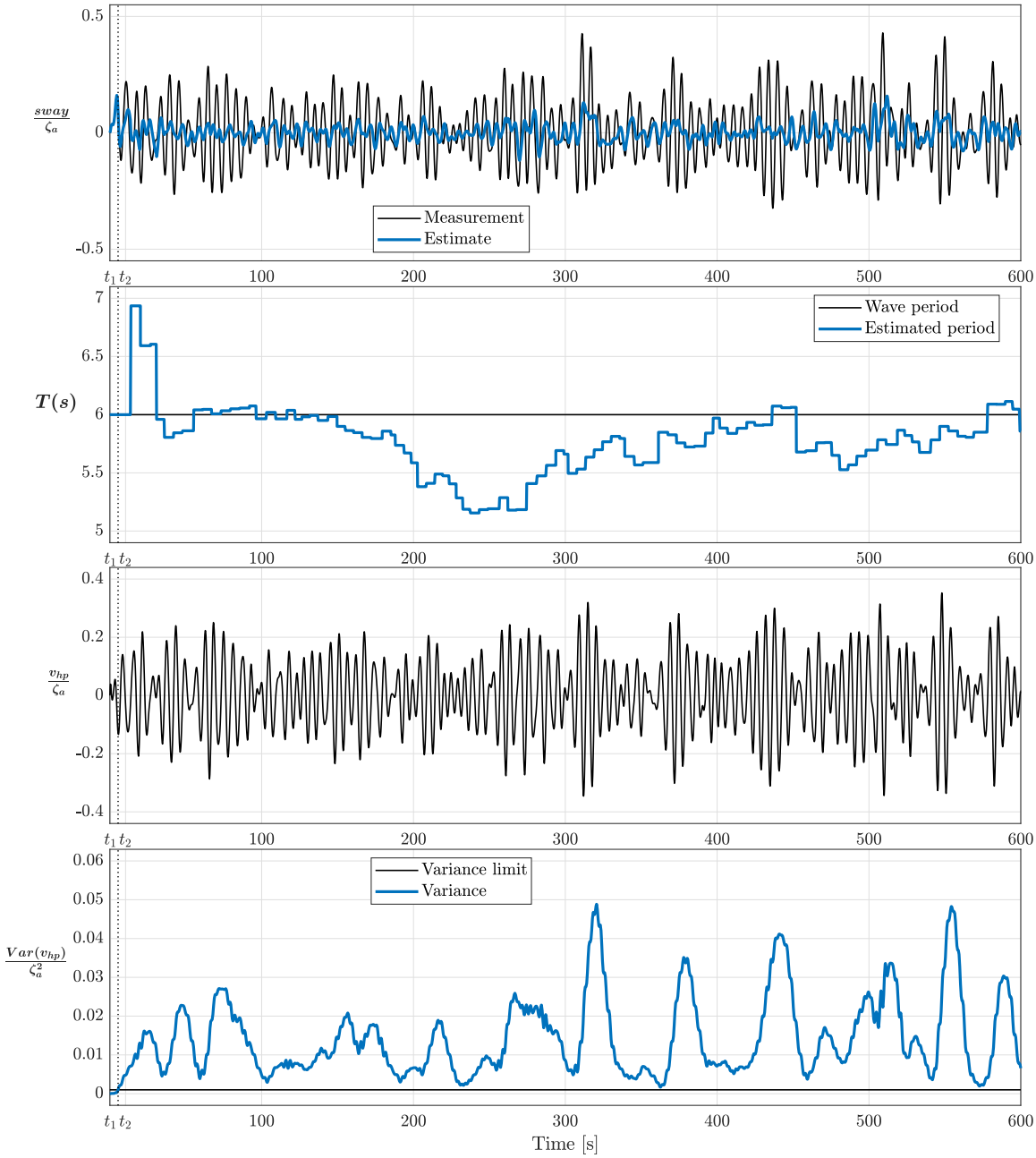

Figure 13: Observer and frequency estimator signals for JONSWAP irregular waves.

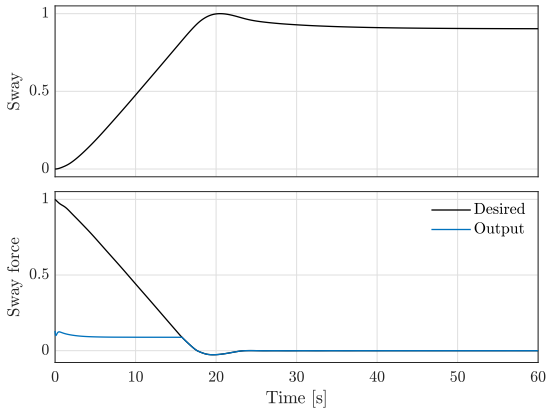

Figure 14: Normalized step response in sway.

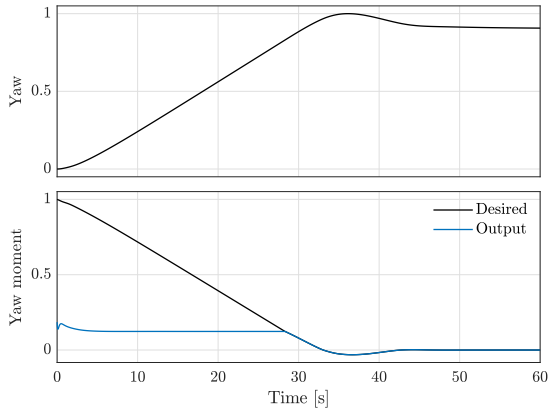

Figure 15: Normalized step response in yaw.

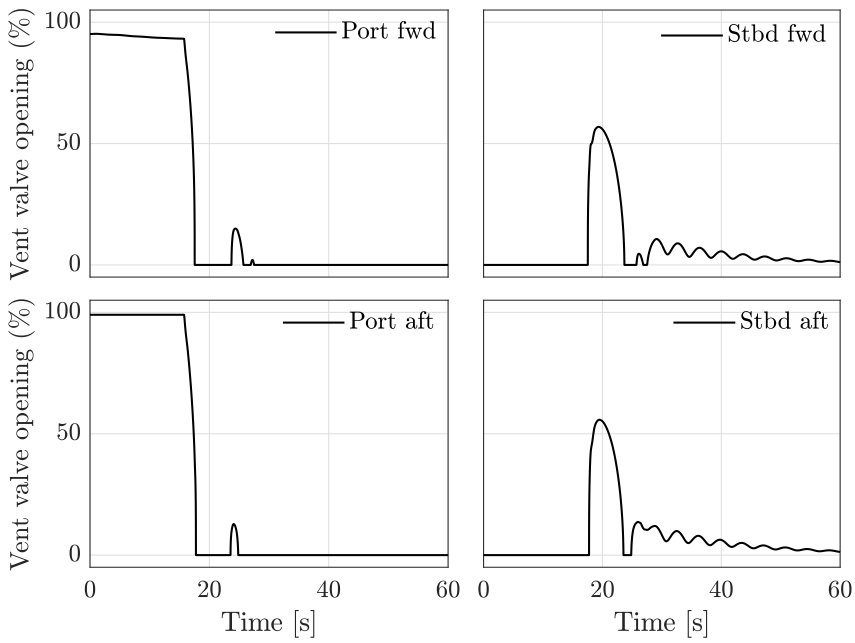

Figure 16: Vent valve positions for sway step response.

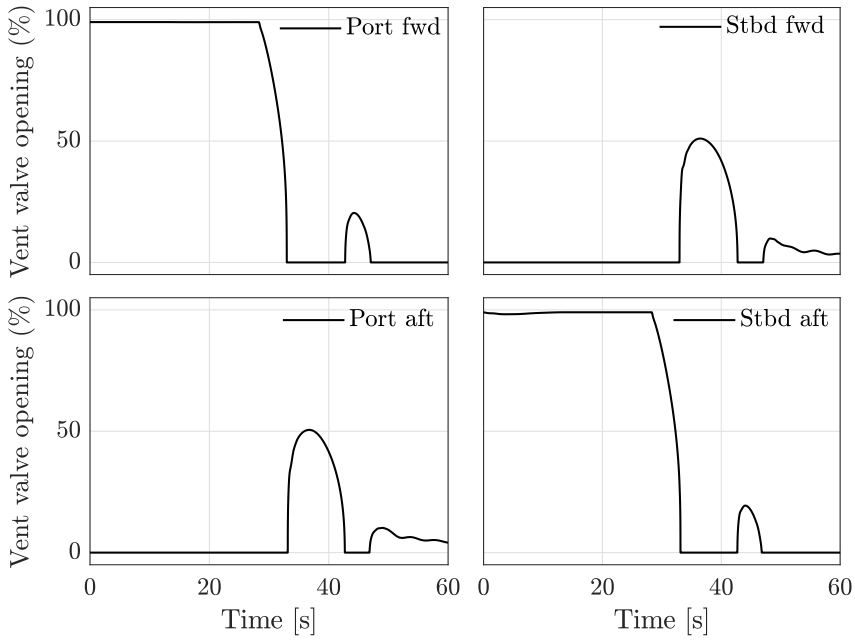

Figure 17: Vent valve positions for yaw step response.

6.1.3 Chattering compensation

For small vent valve openings, the output from the thrust allocation is affected by chattering. However, by implementing a simple chattering compensation, the chattering is removed without having adverse effects on the control system. Fig. 18 shows the difference in the commanded valve positions with and without the chattering compensation when the SES is initialized with a sway offset of 0.001m. The sway response with and without the compensation is shown in Fig. 19. From these results, it may appear that the chattering compensation has an important influence on the response of the SES. However, by initializing the SES with a 0.5m offset, it is seen from Figs. 21 and 20 that the chattering compensation has a negligible effect on the control system.

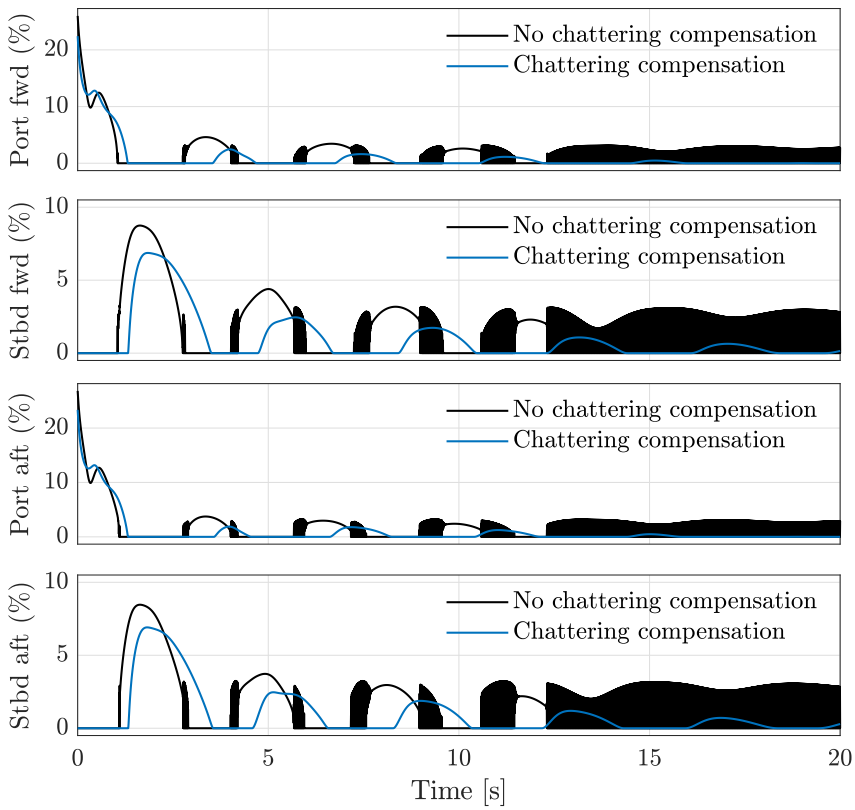

Figure 18: Vent valve positions with and without chattering compensation for a small sway reference offset.

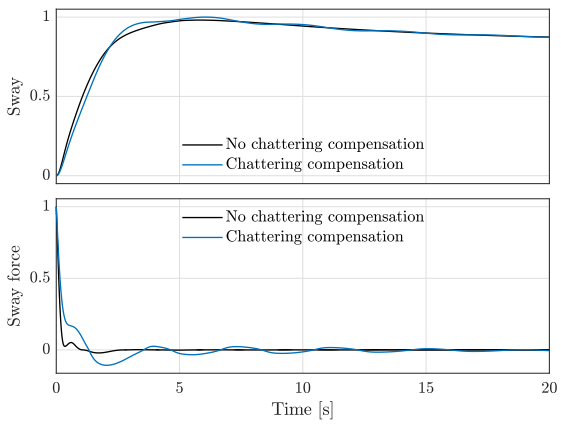

Figure 19: Normalized sway response with and without chattering compensation for a small sway reference offset.

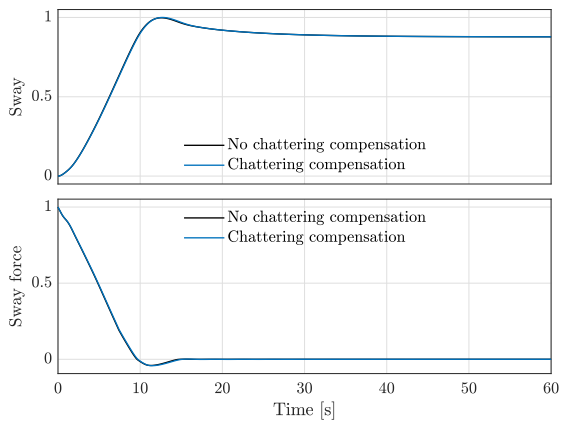

Figure 20: Sway response with and without chattering compensation for sway reference offset.

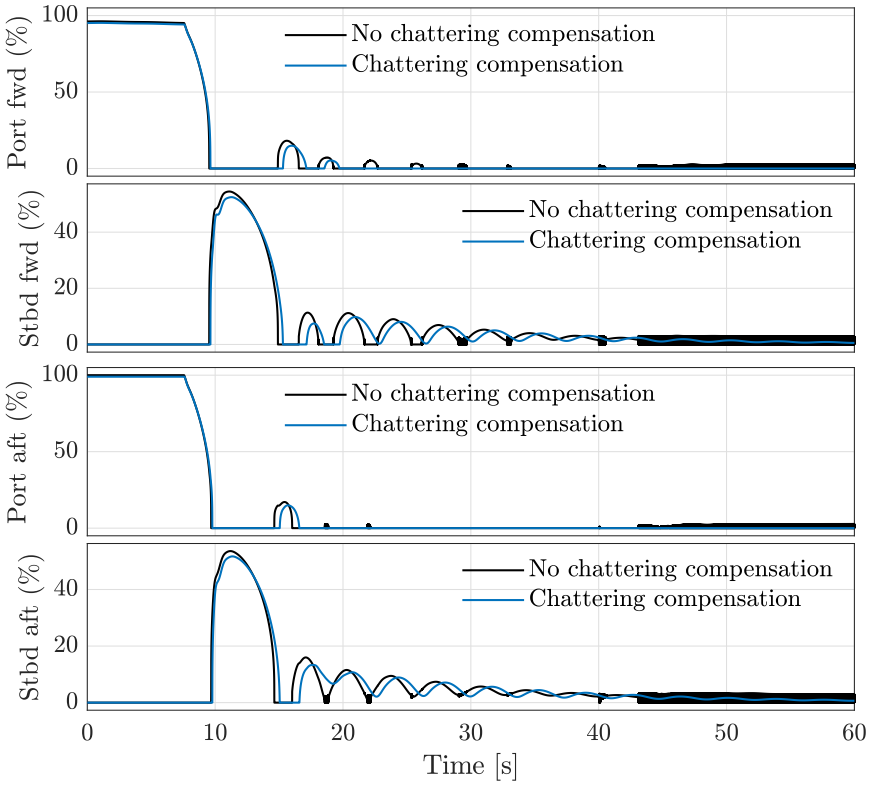

Figure 21: Vent valve positions with and without chattering compensation for sway reference offset.

6.1.4 Constant force

The response, commanded force, and allocated vent valve openings When the SES is exposed to a constant force coming from a 45° yaw angle are shown in Figs. 22, 23 and 24. Initially, the SES is pushed to the port side which causes the port valves to be opened and the SES is pushed back to the reference position. From Figs. 22 and 23 it is seen that the integral term of the PID stabilizes at a non-zero constant value and is compensating the constant exciting force, while the proportional term converges to zero.

The port vent valves follow the commanded force and stabilize at a constant non-zero value, while the starboard vent valves are closed throughout the simulation (Fig. 24). Note also that the pressure stabilizes at a low value when the two port vents are almost fully open, compared to e.g. the case when the SES only has an initial reference offset (Figs. 16 and 17).

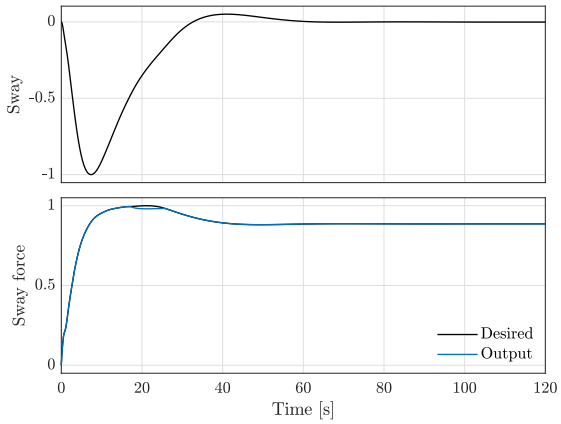

Figure 22: SES sway response when exposed to a constant force coming from 45°.

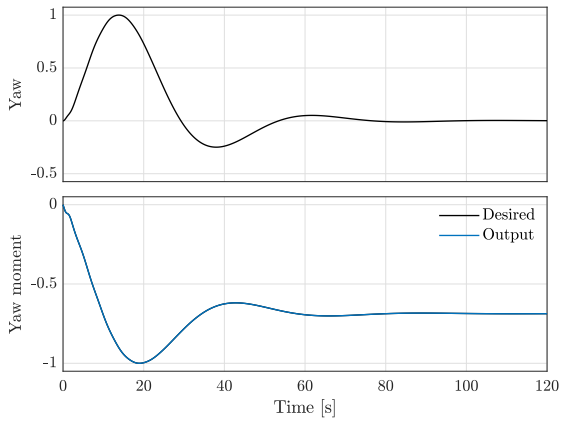

Figure 23: SES yaw response when exposed to a constant force coming from 45°.

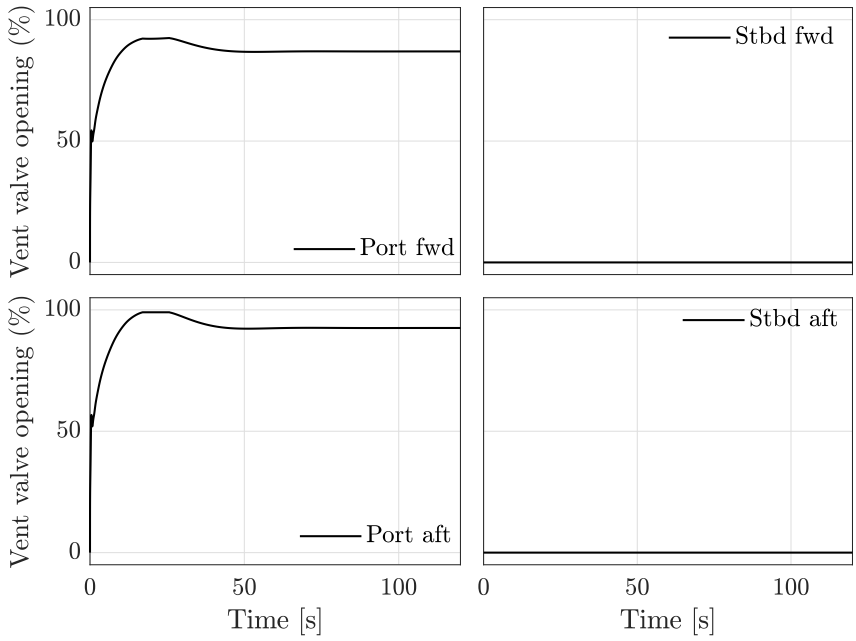

Figure 24: Vent valve positions when exposed to a constant force coming from 45°.

6.1.5 Waves

The response of the SES, when exposed to regular waves with period $8s$ coming from a 45° yaw angle, is shown in Figs. 25, 26 and 27. In waves, the effect of the wave volume pumping on the excess pressure in the cushion becomes clear (Fig. 27) as there are some high-frequency variations in the pressure. Since the pressure is proportional to the thrust force, the pressure variations will is reflected in vent valves with large openings. However, if the vent valves used for the sway-yaw control are the same as the ones used for the RCS, this is not a problem as the valves are actuated with a much higher frequency then what is the case here. If this is not the case and the vent valves cannot handle the pressure variations one can avoid this problem by passing the pressure measurements through a lowpass filter.

6.1.6 Capability

To determine the performance of the control system in a range of sea states, the capability of the system has been tested in simulation with incoming waves at every 10° from 30° to 150°. The capability of the system is defined at the wave height where the SES starts to drift off position. Fig. 28 shows the capability in regular waves for three different wave periods $T_l < T_1 < T_2 < T_3 < T_h$, where T_l and T_h are the lower and upper design wave periods, respectively.

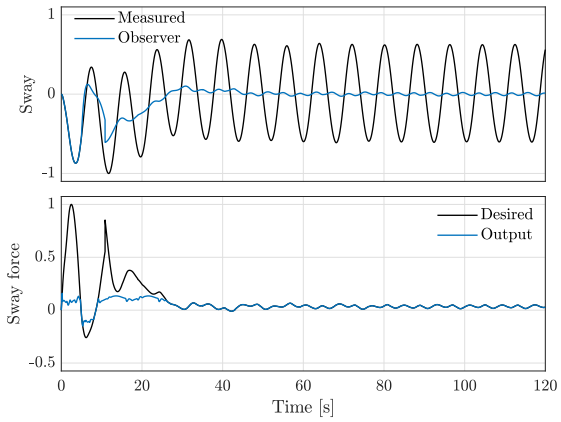

Figure 25: Normalized sway response when exposed to 8s regular waves coming from 45°.

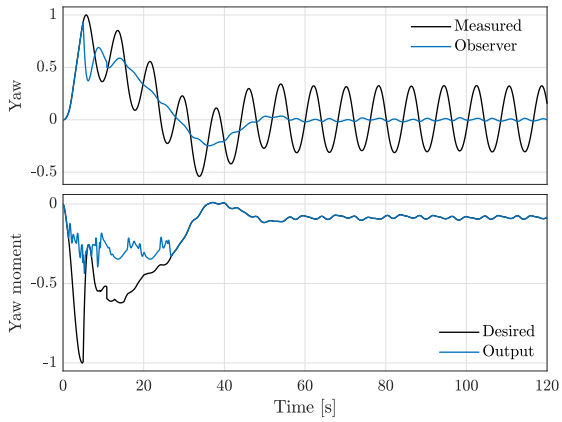

Figure 26: Normalized yaw response when exposed to 8s regular waves coming from 45°.

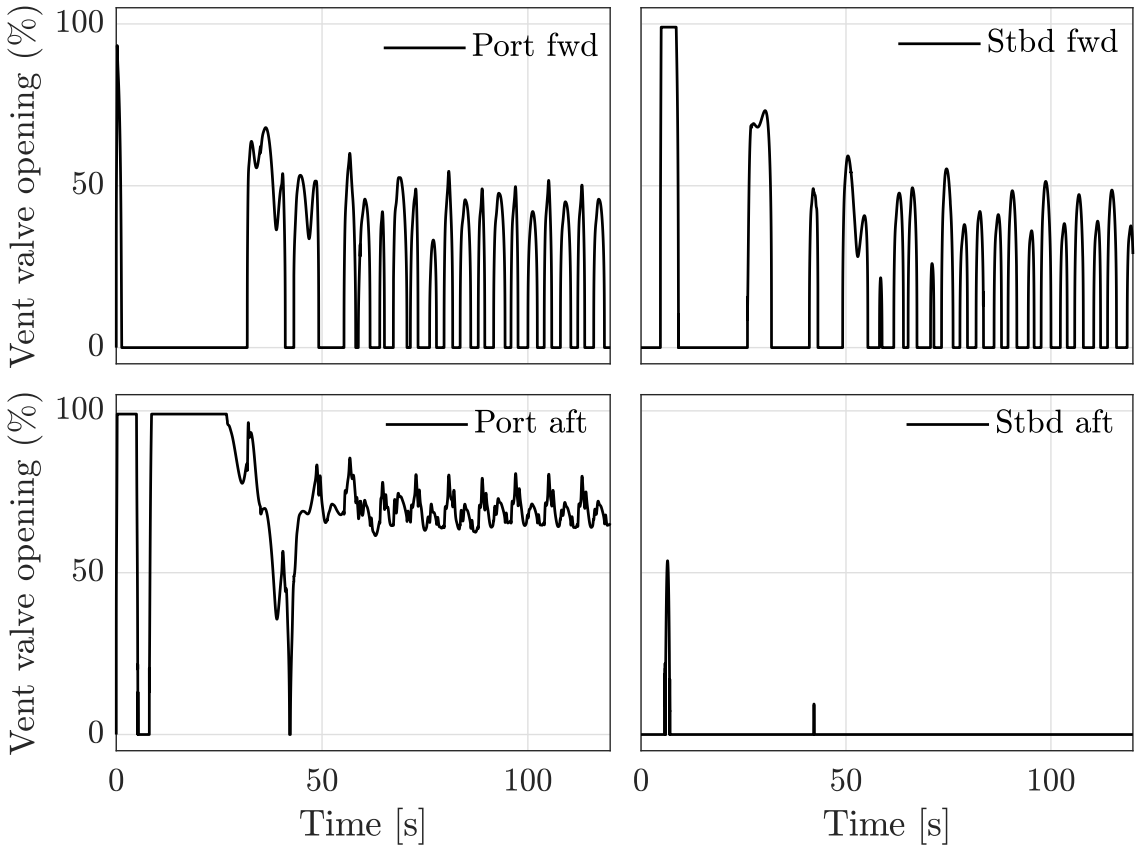

Figure 27: Vent valve positions when exposed to 8s regular waves coming from 45°.

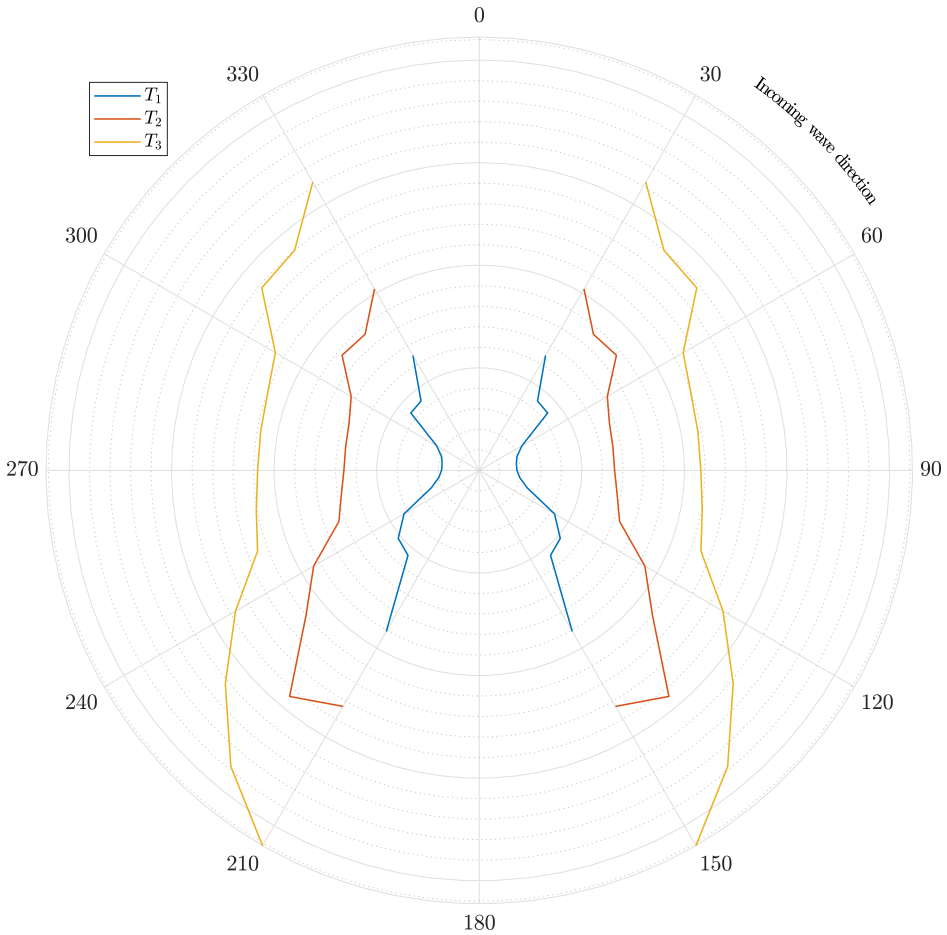

Figure 28: Capability of vent sway yaw control system for three different wave periods.

6.1.7 Vent valve bias

When the vent valves have a constant bias ($u_{cmd,bias}$) the commanded vent valve positions may be negative. The vent valve openings are shown for a case when the SES is initiated with an initial sway and yaw reference offset in Fig. The commanded vent valve positions for a case where the SES is initiated with a sway and yaw reference offset (u^*_{cmd}) and the output when the bias is added ($u^*_{cmd} + u_{cmd,bias}$) are shown in Fig. 29. Initially, only the port forward vent valve is open, while the control system commands the other valves to negative values such that the total effect is that they are closed. This creates a positive sway force and yaw moment. As the SES converges to its reference position, the control system commands zero vent valve opening and the final valve openings converge to the 40% bias.

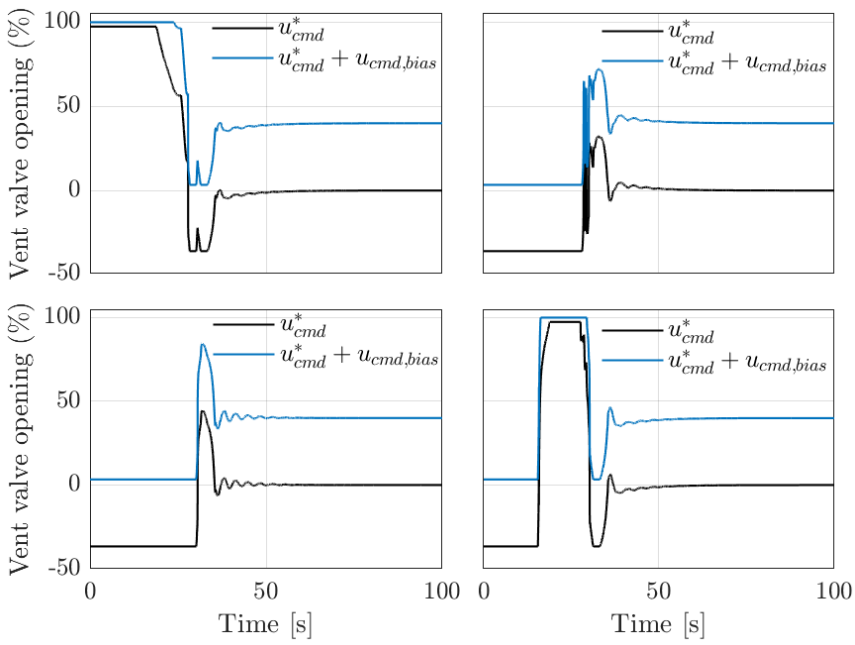

Figure 29: Vent valve positions with 1m sway reference offset, 10° yaw reference offset and 40% vent valve bias.

6.2 Experimental tests

Sway and yaw positions from a test performed with regular waves and current coming in from $-45°$, measured from the bow, are shown in Fig. 30 and 31. The estimated sway and yaw positions are the measured positions passed through the notch filter. At $t = 0$, the waves are initiated and the vessel starts to oscillate with the waves while drifting towards starboard. At approximately $t = 135s$, the control system is turned on and the vessel is pushed back towards the reference position. Due to the offset between the estimated sway position and the mean sway position, the SES is brought a little too far to the port side. Fig. 32 and 33 show the sway position and the vent valve openings around the time when the control system is switched on. Before the control system is switched on, the vent

valves are at a bias of 55%. When the control system is switched on, the starboard valves are opened to provide force directed to the port side. The difference in valve openings on the starboard and port side is to control the yaw angle.

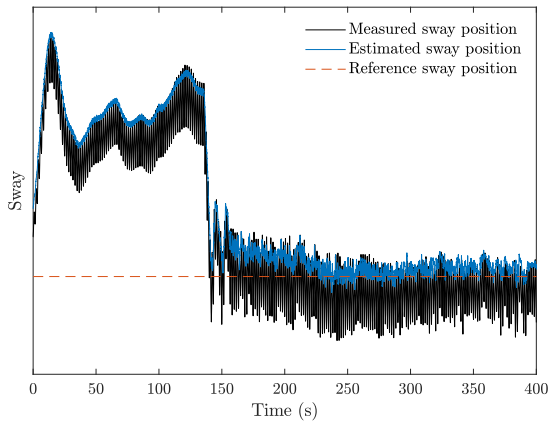

Figure 30: SES sway position with waves and current coming in at $-45°$ from the bow.

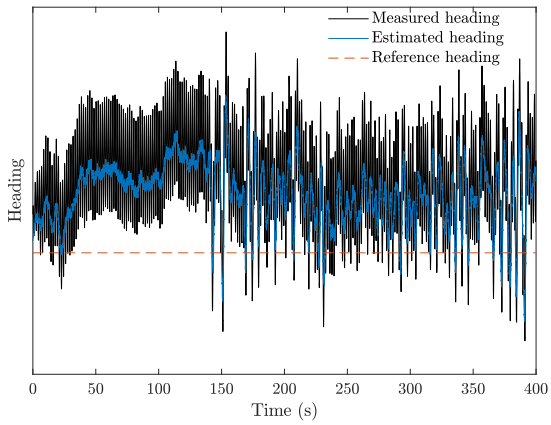

Figure 31: SES heading with waves and current coming in at $-45°$ from the bow.

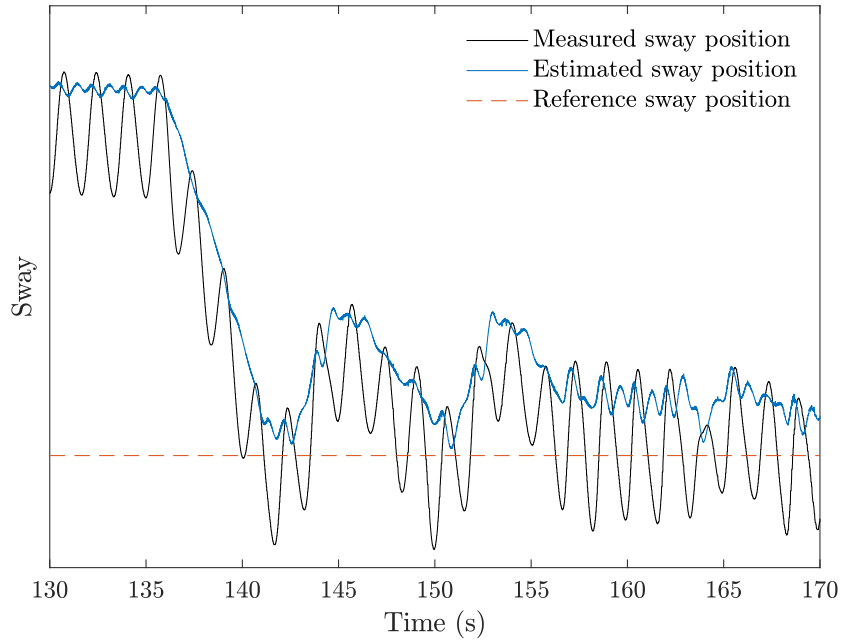

Figure 32: Sway with waves and current coming in at $-45°$ from the bow.

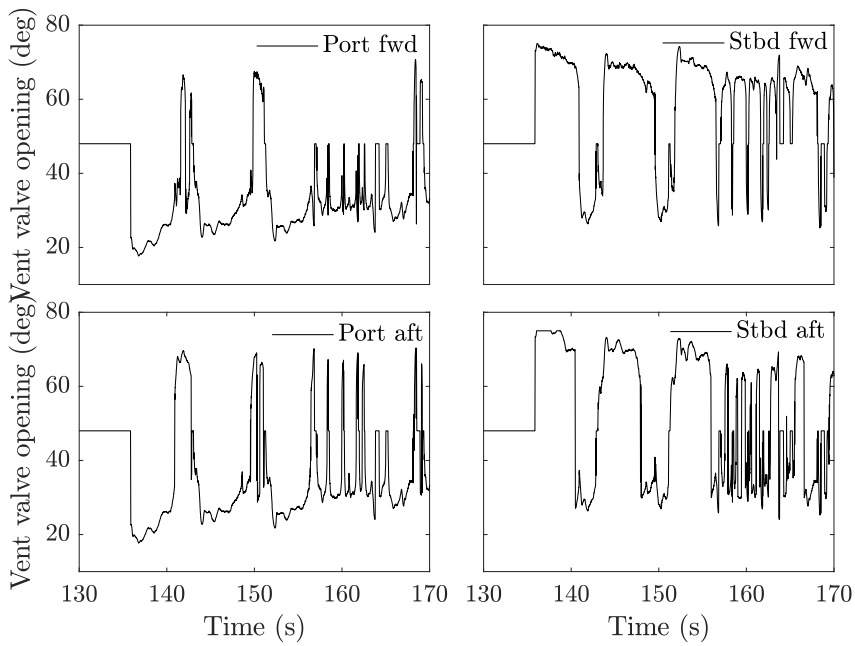

Figure 33: Vent valve position with waves and current coming in at $-45°$ from the bow.

6.3 Thrust force

6.3.1 Orifice coefficient

The calculated orifice coefficient from the CFD analysis and experimental tests are shown in Fig. 34. For valve angles above 70°, the orifice coefficient is between 0.7 and 1, which is as expected and in line with the values given by [25]. However, for lower angles, the orifice coefficient increase beyond 1. From the definition of c_n, it is not physically possible for it to exceed 1 since this would mean that pressure is added to the system, not lost. This is likely because the valves change the direction of the flow, which does not happen with flow through an orifice. Also, the orifice coefficients from scale model A is higher for most of the opening angles. By the previous reasoning, this makes sense since the valves on model A turn in the same direction. This causes the flow to deviate more from the assumed orifice flow.

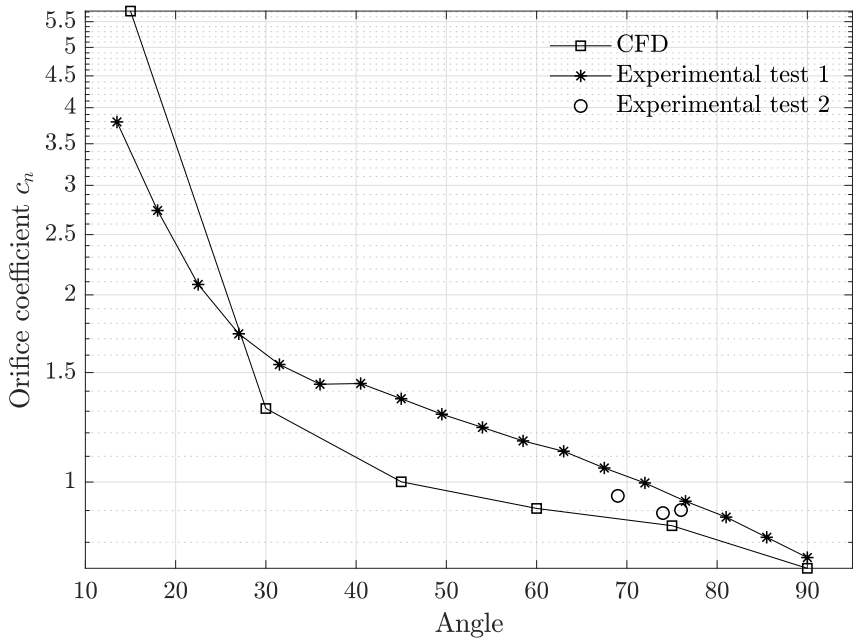

Figure 34: Orifice coefficient obtained from CFD analysis and experimental test.

6.3.2 Loss coefficient

The calculated loss coefficient from the CFD analysis and experimental tests are shown in Fig. 35. The loss coefficients are not far from having an exponential relationship with the valve angle. The valve used in the CFD analysis is modeled based on the valve on model B and these loss coefficients match quite well. The loss coefficient for the vent valve on model A is lower, especially at low opening angles. This is likely because the valve on model A does not seal the vent at zero opening and that the louvers used in each valve are much thinner than the ones used on model B and in the CFD analysis.

The loss coefficients that are shown in 35 are for the complete vent valve system. For the CFD analysis, it is possible to find the valve loss coefficient by simulating the flow without the valve. The loss coefficient obtained then is approximately 1. Since the total loss coefficient of the first model is very low at full opening (0.86), it is assumed that the loss coefficient of model A without valve is 0.76.

When subtracting the constant loss coefficient, the valve loss coefficient is obtained. These values have been fitted to an equation on the form

$$\frac{1}{K_v} = \alpha \exp\left(\frac{\pi\beta\theta}{180}\right) \tag{67}$$

where θ is measured in degrees and α and β are parameters. The calculated and fitted values for the valve loss coefficient are shown in Fig. 36.

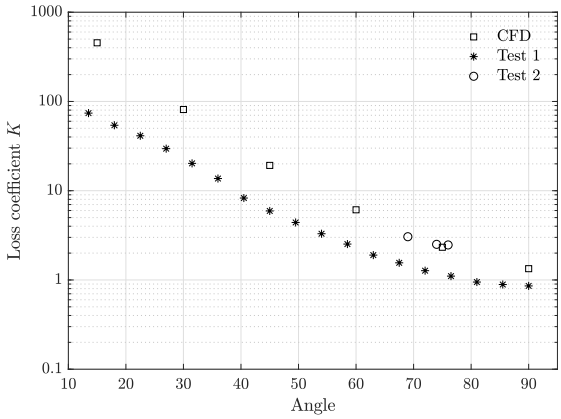

Figure 35: Loss coefficient K for valve opening angle.

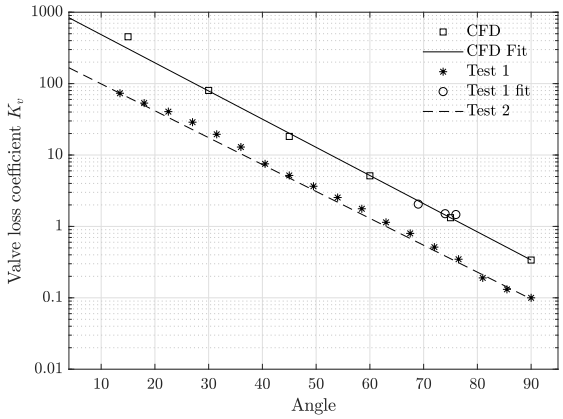

Figure 36: Valve loss coefficient K_v for valve opening angle.

6.3.3 Vent valve force

The vent valve force obtained from the CFD analysis is compared with thrust model 1 (9) and thrust model 2 (16) in Fig. 37. Fig. 38 shows the two models compared with the force obtained from the experimental test performed on scale model A. Assuming an orifice coefficient of 0.8, the first thrust model is not very far off from the CFD analysis but is quite poor compared to scale model A, except at high opening angles. As mentioned previously, this is likely because the valve used for the CFD analysis creates a flow pattern more similar to orifice flow than that of the vent valve on model A.

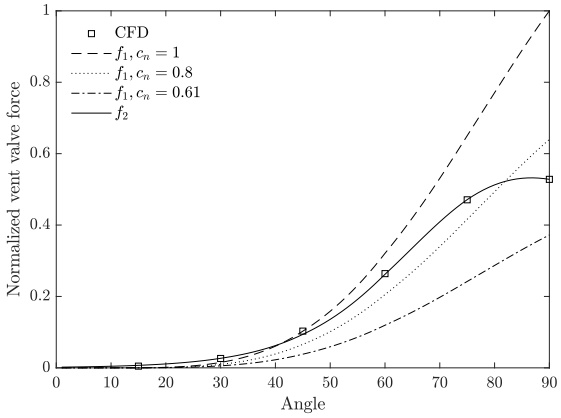

Figure 37: Vent valve force from CFD compared with thrust model 1 and 2.

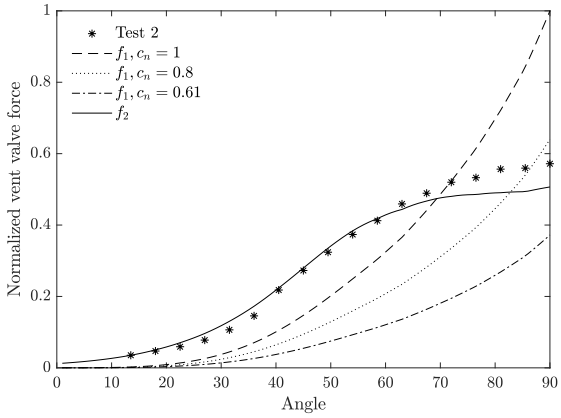

Figure 38: Vent valve force from experimental test on scale model A with thrust model 1 and 2.

7 Discussion

7.1 Sway-yaw control system

The results show that the proposed sway-yaw control system works in simulation and experimental testing. The results obtained from simulation is much better than the results from the experimental testing. This is not surprising considering that there was very little time for experimental testing. Thus, the time available for tuning was very limited and there was practically no time for adapting the system during the experimental testing. One of the issues that could have been fixed if would have allowed was to change the integral saturation. The saturation was implemented such that the integral term in the PID control was unable to increase if any of the vent valves were fully open. In hindsight, the saturation should have been a tunable finite limit. The control system also assumed that the vent valves were operated from 0 to 90°, while in the experimental testing, the vent valves were restricted to operate between approximately 15° and 75°. Finally, the implemented thrust allocation was based on thrust model 1 9 but as the thrust force measurements have shown, this thrust model could give inaccurate force predictions for the vent valve angles used in the experimental tests.

7.2 Design of vent valve DP systems

During the design phase for a SES with DP capability, the main concern with regards to the DP system is the required installed thrust capacity. When installing thrusters, this is quite simple, as the manufacturer provides thrust characteristics and power rating. However, the vent valve thrust is a combination of the fans installed, vent sizes and geometry, and the type of valve used in the vent. Thus, during the initial design phase the main concern is to be able to estimate the thrust produced by the vents. To this end, the following section derives an analytic expression to estimate

the force from a vent valve system.

The fan thrust characteristic is provided by the manufacturers. The airflow into the cushion from one fan may be modeled on the form

$$q_{in} = aq_{max}\left(\frac{p_{max} - p}{p_{max}}\right)^{1/b} \tag{68}$$

where q_{max} and p_{max} are design operational limits of the fan and a and b are used to fit (68) to the fan thrust characteristics provided by the manufacturer. Using the second thrust model, the airflow out of a vent is

$$q_{out} = \sqrt{\frac{2p}{\rho(1 + K(\theta))}}A_v \tag{69}$$

Now, consider a SES with n_v valves on port and starboard side. The total airflow out is

$$Q_{out} = n_v q_{out} \tag{70}$$

and the total airflow in from n_f fans, assuming $a = 1$ and $b = 2$, is

$$Q_{in} = n_f q_{max}\sqrt{\frac{p_{max} - p}{p_{max}}} \tag{71}$$

By equating the airflow out (70) and airflow in (71) an analytic expression for the cushion pressure is obtained as

$$p = \frac{n_f^2 q_{max}^2 p_{max}\rho(1 + K(\theta))}{2n_v^2 A_v^2 p_{max} + n_f^2 q_{max}^2 \rho(1 + K(\theta))} \tag{72}$$

The total force in sway now becomes

$$F_{sway} = 2n_v A_v \frac{n_f^2 q_{max}^2 p_{max}\rho}{2n_v^2 A_v^2 p_{max} + n_f^2 q_{max}^2 \rho(1 + K(\theta))} \tag{73}$$

The above equation can be used in the design phase of a vent valve DP system. For example, the optimal vent area at maximum vent valve opening may be found by

$$\frac{\partial F_{sway}}{\partial A_v} = 0 \tag{74}$$

which gives

$$A_{v,optimal} = \frac{n_f q_{max}}{n_v p_{max}}\sqrt{\frac{\rho(1 + K(90))}{2}} \tag{75}$$

As an example, consider a SES with vent valves on port and starboard side and 6 fans with design limits $p_{max} = 10000$Pa and $q_{max} = 100\text{m}^3$. The maximum sway force when installing 2 or 4 vent valves on each side is shown in Fig. 39 for varying vent size.

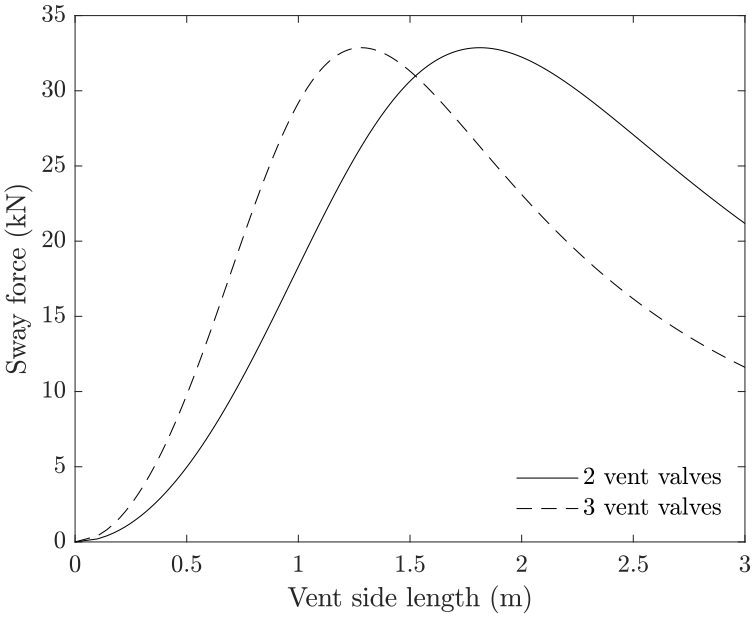

Figure 39: Maximum sway force when installing 2 or 4 vent valves on each side.

8 Conclusion

A sway-yaw control system for a SES using the thrust force obtained by exploiting the pressure difference between the cushion and atmosphere has been proposed. Simulations and experimental testing have been used for testing and verification. In addition, the available thrust force from the vent valves have been investigated and a thrust force model has been proposed. The control system and the principle of using thrust force from vent valves have been shown to work. Although implementation details would need to be addressed, the control system should work on a full size SES. The benefit of the control system is that it is so simple that it requires no alternations when it has been tuned properly and since there are very few parameters in the control system, tuning should be relatively simple.

Both thrust models provide a practical estimate of the thrust force from a vent valve at maximum valve opening, assuming an orifice coefficient of 0.8 for the first thrust model. The first model does not seem to give an accurate thrust force estimate unless the valve is almost completely open. Using the second thrust model seems to give very good predictions of thrust force. The second model relies on valve loss coefficient data, but this is usually supplied by the valve manufacturer. The agreement between CFD analyses and experimental tests indicate that in lack of valve data, a simple CFD analysis may be used to find the valve loss coefficients.

Although more work on this subject would provide useful insight, especially with regards to the generated thrust force and the geometry and layout of the vent valve system, the proposed system could serve as a basis for implementation on a full size SES.

References

[1] *Helse, sikkerhet og sikring.* https://www.equinor.com/no/how-and-why/health--safety-and-security.html. Accessed: 2019-05-20.

[2] Petroleumstilsynet. *Risikonivåi petroleumsvirksomheten.* Tech. rep. Petroleumstilsynet, 2018.

[3] Edward A. Butler. "The Surface Effect Ship". In: *Naval Engineers Journal* 97.2 (Feb. 1985), pp. 200–253. DOI: 10.1111/j.1559-3584.1985.tb03399.x.

[4] A.J. Sørensen and O. Egeland. "Design of ride control system for surface effect ships using dissipative control". In: *Automatica* 31.2 (Feb. 1995), pp. 183–199. DOI: 10.1016/0005-1098(94)00090-6.

[5] DNV. *DNV Ship rules Pt.6 Ch.7 - Dynamic Positioning Systems.* Tech. rep. DNV, 2011.

[6] O. Olubitan et al. "An investigation and statistical analysis into the incidents and failures associated with dynamic positioning systems". In: *Safety and Reliability – Safe Societies in a Changing World.* CRC Press, June 2018, pp. 79–85. DOI: 10.1201/9781351174664-10.

[7] Hubert Fay. *Dynamic Positioning Systems.* Technip Editions, 1989. ISBN: 2-7108-0580-4. URL: https://www.amazon.com/Dynamic-Positioning-Systems-Hubert-Fay/dp/2710805804?SubscriptionId=AKIAIOBINVZYXZQZ2U3A&tag=chimbori05-20&linkCode=xm2&camp=2025&creative=165953&creativeASIN=2710805804.

[8] Thor I Fossen and Jann Peter Strand. "Passive nonlinear observer design for ships using lyapunov methods: full-scale experiments with a supply vessel". In: *Automatica* 35.1 (Jan. 1999), pp. 3–16. DOI: 10.1016/s0005-1098(98)00121-6.

[9] Asgeir J. Sørensen. "A survey of dynamic positioning control systems". In: *Annual Reviews in Control* 35.1 (Apr. 2011), pp. 123–136. DOI: 10.1016/j.arcontrol.2011.03.008.

[10] Trong Dong Nguyen, Asgeir J. Sørensen, and Ser Tong Quek. "Design of hybrid controller for dynamic positioning from calm to extreme sea conditions". In: *Automatica* 43.5 (May 2007), pp. 768–785. DOI: 10.1016/j.automatica.2006.11.017.

[11] Fossen. *Guidance Control of Ocean Vehicles.* John Wiley & Sons, Aug. 23, 1994. 496 pp. ISBN: 0471941131. URL: https://www.ebook.de/de/product/3597693/fossen_guidance_control_of_ocean_vehicles.html.

[12] Tor A. Johansen et al. "Optimal constrained control allocation in marine surface vessels with rudders". In: *Control Engineering Practice* 16.4 (Apr. 2008), pp. 457–464. DOI: 10.1016/j.conengprac.2007.01.012.

[13] Øyvind F. Auestad et al. "Boarding control system for improved accessibility to offshore wind turbines: Full-scale testing". In: *Control Engineering Practice* 45 (Dec. 2015), pp. 207–218. DOI: 10.1016/j.conengprac.2015.09.016.

[14] Vegard Vamråk et al. "Robust Lateral Control of a Surface Effect Ship using H∞ Mixed Sensitivity Synthesis". In: *IFAC-PapersOnLine* 49.23 (2016), pp. 540–545. DOI: 10.1016/j.ifacol.2016.10.491.

[15] G. Zames. "Feedback and optimal sensitivity: Model reference transformations, multiplicative seminorms, and approximate inverses". In: *IEEE Transactions on Automatic Control* 26.2 (Apr. 1981), pp. 301–320. DOI: 10.1109/tac.1981.1102603.

[16] Per Sondre Sodeland. "Combined Dynamic Positioning and Optimal Wave Frequency Motion Damping of Surface Effect Ship". MA thesis. Department of Marine Technology, Norwegian University of Science and Technology, 2015.

[17] Paul Kaplan, James Bentson, and Sydney Davis. "Dynamics and Hydrodynamics of Surface-Effect ships". In: *SNAME Transactions* 89 (1981), pp. 211–247.

[18] Sverre Steen. *Cobblestone Effect on SES*. Norges Tekniske Hœgskole, 1993.

[19] M. J. Hinchey P. A. Sullivan F. Gosselin. "Dynamic Response of an Air Cushion Lift Fan". In: *Intersociety High Performance Marine Vehicle Conference and Exhibit*. 1992.

[20] Frank M. White. *Fluid Mechanics*. McGraw-Hill Education - Europe, Jan. 16, 2015. 864 pp. ISBN: 0073398276. URL: https://www.ebook.de/de/product/24169402/frank_m_white_fluid_mechanics.html.

[21] Klaus Hasselmann et al. "Measurements of wind-wave growth and swell decay during the Joint North Sea Wave Project (JONSWAP)". In: *Deut. Hydrogr. Z.* 8 (Jan. 1973), pp. 1–95.

[22] DNV. *DNV-RP-C205 ENVIRONMENTAL CONDITIONS AND ENVIRONMENTAL LOADS*. Tech. rep. DNV, 2010.

[23] Thor I. Fossen. *Handbook of Marine Craft Hydrodynamics and Motion Control*. Wiley-Blackwell, Apr. 13, 2011. ISBN: 1119991498. URL: https://www.ebook.de/de/product/15427426/handbook_of_marine_craft_hydrodynamics_and_motion_control.html.

[24] Hassan K. Khalil. *Nonlinear Systems*. PEARSON, 2001. ISBN: 0-13-067389-7.

[25] Odd M. Faltinsen. *Hydrodynamics of High-Speed Marine Vehicles*. CAMBRIDGE UNIV PR, Aug. 29, 2012. 454 pp. ISBN: 0521845688. URL: https://www.ebook.de/de/product/4407419/odd_m_faltinsen_hydrodynamics_of_high_speed_marine_vehicles.html.

NTNU

Norwegian University of
Science and Technology